9

Magnetical Response and Mechanical Properties of High Temperature Superconductors, $YBaCu_3O_{7-X}$ Materials

J.J. Roa[1,*], F.T. Dias[2] and M. Segarra[3]
[1]*Institut P' (UPR 3346), Département de Physique et Mécanique des Matériaux, CNRS - Université de Poitiers – ENSMA, SP2MI - Téléport 2 - BP 30179, F-86962 Futuroscope, Chasseneuil Cedex*
[2]*Federal University of Pelotas, Physics and Mathematics Institute, Department of Physics,*
[3]*DIOPMA Centre. Universitat de Barcelona, Facultat de Quimica, Departament de Ciència dels Materials i Enginyeria Metal·lúrgica, Barcelona*
[1]*France*
[2]*Brazil*
[3]*Spain*

1. Introduction

Since the discovery of the second generation High Superconductor Materials (2G-HTSC) in 1986, their magnetic properties have been widely studied by different research groups around the world. During the last years, the mechanical properties at micro-/ and nanometric scale are starting to be studied in order to know and improve the durability of conventional devices.

In this book chapter, we would like to focus our attention on the magnetical response and also the mechanical properties of 2G-HTSC.

In relation to the magnetic response, the Meissner effect is one important signature of the superconductivity. In this case, a diamagnetic response is observed due to exclusion of the magnetic flux of the interior of the superconducting material when the temperature is below the critical temperature. This important property allows to distinguish a superconducting material from a conducting one. But in several cases the superconducting materials exhibit a paramagnetic response instead of the conventional diamagnetism. This effect is frequently called *paramagnetic Meissner effect (PME).* In this case, the magnetic flux is not expelled, and a paramagnetic state can be originated. This effect is observed in several magnetic field regimes, and in some cases the paramagnetic response increases with the applied magnetic field, but in others the paramagnetic response decreases when the magnetic field increases.

The paramagnetic Meissner effect (PME) was first observed in polycrystalline samples of high temperature superconductors. The discovery of this effect has originated an enormous effort of investigation by several groups around the world and several theories and models have been proposed to explain this interesting and controversial behavior, but without a

conclusive understanding yet. One of the first interpretations is based on the occurrence of Josephson π junctions between superconducting grains into the sample, and in this case the superconducting samples showing the PME can be modeled as a Josephson medium where the π junctions are randomly distributed.

Some experimental results have motivated the proposal of mechanisms based on flux trapping and flux compression into the samples, and a non-equilibrium compressed flux states can be stabilized by inhomogeneously cooling the sample, thus yielding to a paramagnetic response. The formation of a giant vortex state on the sample, or the flux capture by samples with a particular shape, may produce a strong compression of the trapped flux in their interior. Several groups have used models based on these ideas to explain their results mainly when high magnetic fields are applied.

Other models based on arrays of multiply-connected superconductors have been proposed to explain the PME. Josephson junctions are taken into account and a paramagnetic response appears when inner currents may flow through these junctions under special conditions. Many groups have pointed that the PME observed in granular superconductors can be described as an intrinsic effect of multiply-connected superconductors, since the granularity emulates a network of Josephson junctions.

An important result observed in superconducting samples that exhibit the PME is the anomalous time-dependence on the magnetization. In some cases, the paramagnetic moments obtained after field cooling process relax monotonically to increasingly positive values. Some results show that this tendency remains unaltered for large time intervals. In other cases, the relaxation may show a change of sign in the magnetization from negative to positive. This behavior is opposite to expectations based on a flux-creep scenario, and some models have been proposed in order to explain this anomalous effect.

One of the sections of this chapter is dedicated to a review of the experimental results and main models and ideas about the paramagnetic Meissner effect in high-Tc materials. A special attention to results observed in $YBa_2Cu_3O_{7-x}$ superconductor prepared by melt-textured techniques will be paid. These materials are very important to technological applications, and in some cases the observed PME is very strong. In relation to melt-textured samples, the importance of the Y_2BaCuO_5 (Y-211) phase added during the growth is also discussed in order to connect with the PME causes.

Concerning the mechanical properties, attention will be focused on the following: hardness, Elastic modulus, toughness fracture and the stress-strain curve, taking into account the different works published since the discovery of this material. However, their determination at nanometric scale is highlighted, as this technique is very functional and fast, and can give us a lot of information about the mechanical behavior of each phase present in this kind of ceramic materials. The principle of the technique is the evaluation of the response of a material to an applied load, it allows to extract the mechanical properties of an heterogeneous material at very low applied loads. Depending on the tip employed, different equations should be applied to study the response of the material (Oliver and Pharr or Hertz equations for elastic-to-plastic and elastic regimen respectively), and thus calculate the stress-strain curves in order to obtain the yield strength of the material, and conventional parameters like hardness, Elastic modulus and toughness. In this chapter we would like to make a state of the art of the different mechanical properties obtained using hardness tests

up to now of a ceramic superconductor material ($YBa_2Cu_3O_{7-x}$ or Y-123) textured by Bridgman and Top-Seeding Melt Growth techniques. This material presents a phase transition from tetragonal to orthorhombic that promotes a change in its electrical properties, from insulating to superconductor, and that can be achieved by partially oxygenating the material. On the other hand, the structure of the texture material presents a heterogeneous distribution of two different phases: Y-123) as a matrix and Y-211 as quasi spherical inclusions. So, a review and a discussion about the different equations and method employed to isolate the mechanical response for each phase and for the whole material is presented. Finally, the different fracture mechanisms activated during the indentation process such as chipping, or radial cracks at the corners of the imprints will be presented.

1.1 Magnetic response: The paramagnetic Meissner effect

This section is dedicated to the description of the magnetic response exhibited by some superconducting materials, which is known as the paramagnetic Meissner effect.

1.1.1 The Meissner effect

The Meissner effect is one important signature of the superconductivity. In this case, a diamagnetic response is observed due to exclusion of the magnetic flux from inside the superconducting material when the temperature is below its critical temperature. This important property allows us to distinguish a superconducting material from a perfectly conducting material.

Type-II superconductors present a perfect diamagnetism (Meissner effect) just when the magnetic applied field is lower than $H_{C1}(T)$, known as the lower critical field, as showed by **Fig. 1**. Consequently this region is known as Meissner state. For magnetic applied fields higher than $H_{C1}(T)$ but lower than $H_{C2}(T)$, or upper critical field, the magnetic field can penetrate inside the superconductor in the form of vortices. This state is known as mixed state, and the $H_{C1}(T)$ value determines the penetration of the first magnetic flux-line inside the superconductor.

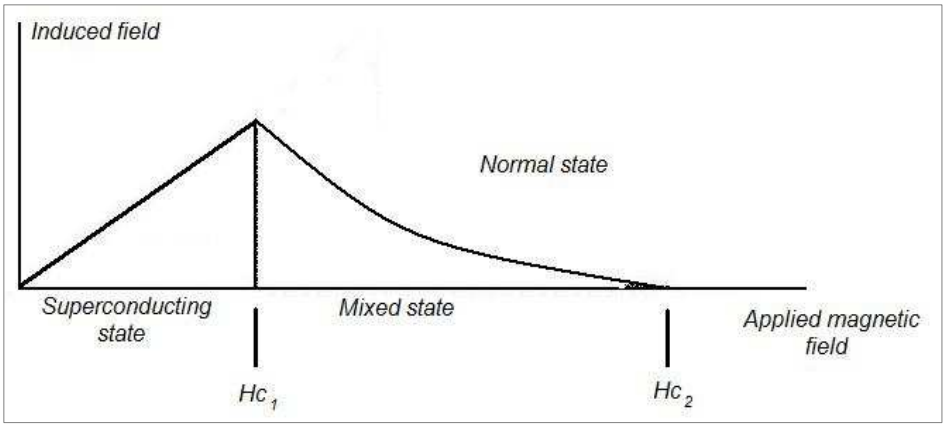

Fig. 1. Magnetic behaviour of a type-II superconductor.

The Meissner effect can be observed by the field-cooled warming (FCW) or field-cooled cooling (FCC) prescriptions. The FCW prescription consists of a first cooling down of the superconducting material to temperatures well below the critical temperature (T_C) in magnetic applied field; then the magnetization can be measured under constant magnetic field while the sample warms up to temperatures above the critical temperature. The FCC prescription is similar, but in this case the magnetization is measured while cooling the sample back to temperatures well below the critical temperature in magnetic applied field. In these conditions the magnetic flux uniformly distributes into the sample, and when the sample is cooled below T_C a diamagnetic moment appears as a consequence of the expulsion of magnetic flux from within it. Due to vortex pinning effects, in general the field-cooled (FC) response is lower than the zero-field cooling (ZFC - diamagnetic shielding) response, as showed by **Fig. 2**.

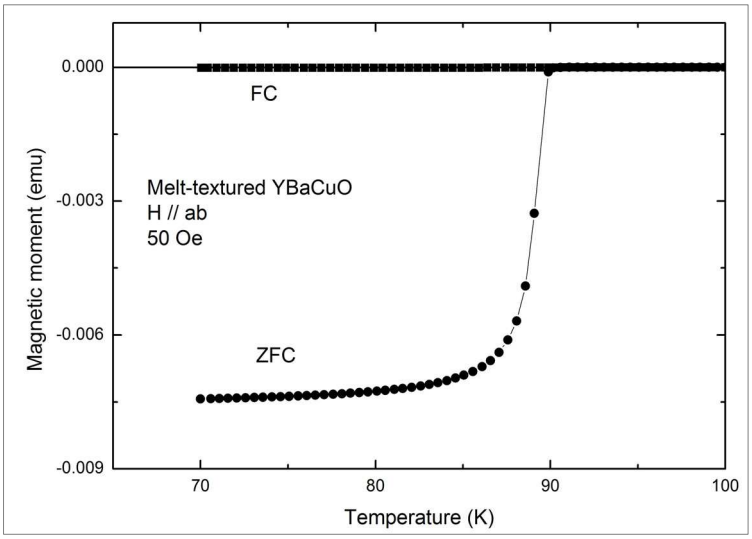

Fig. 2. ZFC and FC curves for a melt-textured $YBa_2Cu_3O_{7-x}$ sample.

1.1.2 Paramagnetic Meissner effect

The Meissner effect is characterized by a diamagnetic response of the superconducting material when a magnetic field is applied, but in several cases this magnetic response in FC experiments can be paramagnetic, challenging the conventional Meissner effect. This effect is known as paramagnetic Meissner effect (PME), but sometimes is called Wohlleben effect in honor of some of its discoverers (Bräuchle et al., 1994; Khomskii, 1994).

The first observations of the PME were reported in a pioneer work by P. Svedlindh et al. (Svedlindh et al., 1989) in the BiSrCaCuO superconductor. The discovery of the PME has prompted an enormous effort of investigation due to the striking contrast of this effect with the expected diamagnetic response. Initially, the effect was credited as an artifact of the measurement procedure (Blunt et al., 1991), but several further results showed that the PME is a genuine response of the superconducting material.

The PME has been observed in several superconducting systems, since low-T_C materials such as Nb (Thompson et al., 1996; Minhaj et al., 1994), high-Tc materials such as $Bi_2Sr_2CaCu_2O_8$ and $YBa_2Cu_3O_{7-x}$ (Braunisch et al., 1992; Dias et al., 2000), exotic systems such as $Ba_{1-x}K_xBiO_3$ (Kim et al., 1996), multiphase In-Sn alloys (Schwartz et al., 2006), $YBa_2Cu_3O_{7-x}$ /$La_{0.7}Ca_{0.3}MnO_3$ superlattices (Arias et al., 2006), organic compounds (Lebed, 2008) and many others. Recently, the PME has been also observed in Pb films by Brandt et al. (Brandt et al., 2011). The effect can be observed in polycrystalline sintered samples (Svendlindh et al., 1989), melt-textured samples (Pureur et al., 2001), single-crystals (Kusmartsev et al., 1997; Dias et al., 2010), alloys (Schwartz et al., 2006) and thin films (Pan et al., 2006; Terentiev et al., 1999) prepared by several techniques.

The PME is qualitatively distinct in relation to the applied magnetic field, and can be observed from few Oe up to several kOe. In some cases the effect decreases when the magnetic field increases, as can be seen in **Fig. 3** for an $YBa_2Cu_3O_{7-x}$ single-crystal. However, in other cases the effect increases when the magnetic field increases, as showed by **Fig. 4** for another $YBa_2Cu_3O_{7-x}$ single-crystal.

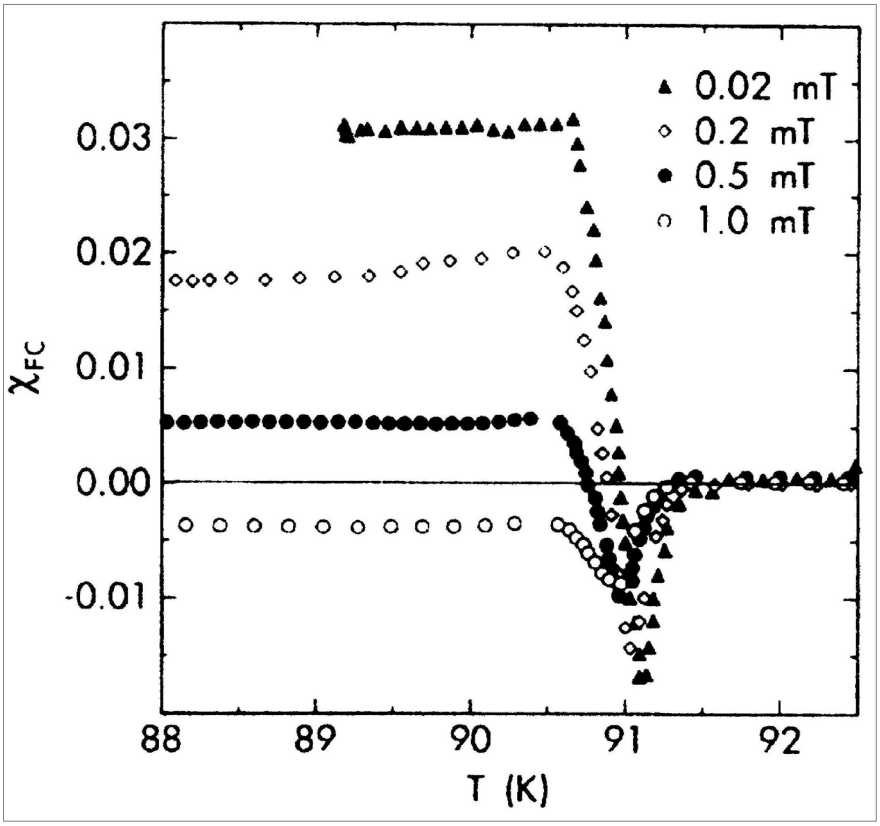

Fig. 3. Magnetic susceptibility in an $YBa_2Cu_3O_{7-x}$ single crystal. The magnetic susceptibility decreases when the magnetic field increases. From Bräuchle et al., 1994.

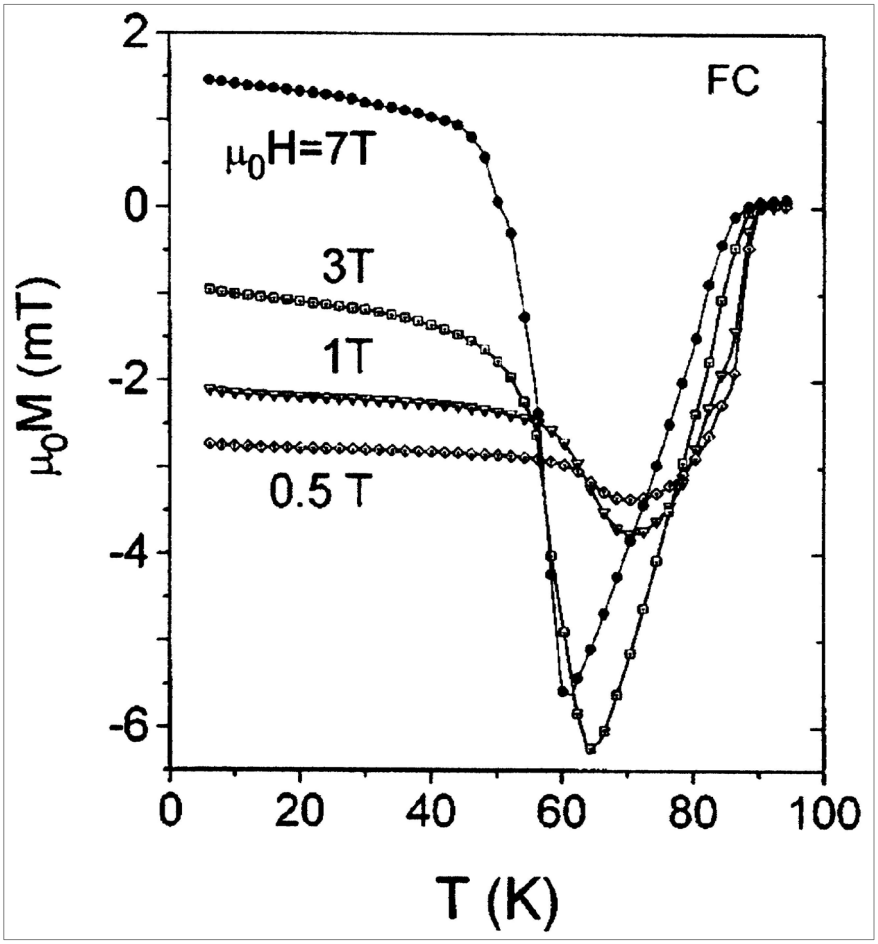

Fig. 4. FC magnetizations in an overdoped $YBa_2Cu_3O_{7-x}$ single crystal. In this case the magnetization increases when the magnetic field increases. From Kusmartsev et al., 1992.

Sometimes the PME presents a curious time dependence of the FC magnetization, as showed by **Fig. 5** for a melt-textured $YBa_2Cu_3O_{7-x}$ sample. In **Fig. 5** a paramagnetic signal was observed when the FC moment relaxes at constant magnetic field and temperature. The inset of this figure shows the sign reversal obtained in a relaxation experiment in the same sample, but cooled under another rate and magnetic field configuration.

It is possible to observe that an originally negative FC moment relaxes towards positive values and reverses sign after a wait time of about 3000 s. The time dependence of the PME has been related by other authors in different superconducting materials (Pan et al., 2006; Terentiev et al., 1999; Dias et al., 2004).

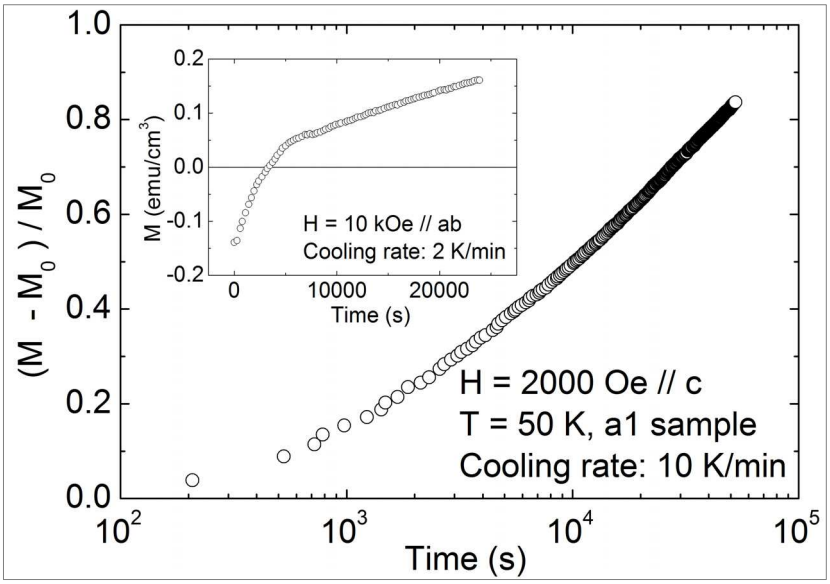

Fig. 5. Time dependence of normalized FC magnetization in a melt-textured $YBa_2Cu_3O_{7-x}$ sample exhibiting the PME. The inset shows the sign reversal obtained in a relaxation experiment in the same sample. From Pureur et al., 2001.

1.1.3 Models and experimental results

The paramagnetic Meissner effect is a controversial and challenging effect that can be observed in a variety of superconducting systems. However, in several cases there is a strong dependence on the applied magnetic field (magnitude and configuration), cooling rate during measurements, time effects, pinning effects, and others circumstances, and hence there is no a definitive model that can explain the paramagnetic moments observed during the FC experiments.

After the first observations of the PME, an enormous effort of investigation has emerged in order to explain this anomalous effect. The initial motivation was given by its interpretation based on the occurrence of π junctions between the superconducting grains in the material (Kusmartsev et al., 1992).

According to this, the sample showing PME may be modeled as a Josephson medium where the π junctions are randomly distributed. Assuming that closed superconducting loops containing an odd number of these anomalous junctions are likely to occur in these networks, spontaneous and polarizable orbital currents may be generated, giving rise to the PME when very low magnetic fields are applied. The required π-phase shifts in the Josephson links were proposed to arise from *d*-wave pairing symmetry in the high-*Tc* superconducting materials (Sigrist & Rice, 1995).

The **Fig. 6** shows PME results obtained in a polycrystalline $Bi_2Sr_2CaCu_2O_8$ sample by Braunisch et al. (Braunisch et al., 1992) and explained on the basis of this model.

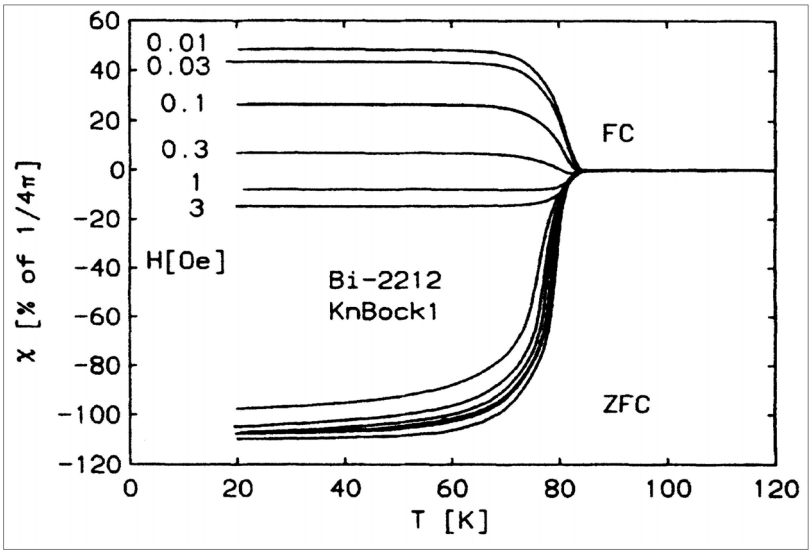

Fig. 6. ZFC and FC signals in a polycrystalline $Bi_2Sr_2CaCu_2O_8$ sample exhibiting the PME. From Braunisch et al., 1992.

Several results can be explained based on this model, specially when low magnetic fields are applied. The concept of polarized orbital currents to explain the low field PME was further developed by studies of the characteristic microstructure of samples showing this effect (Freitag et al., 1999), and by investigations on the time dependence of the paramagnetic moment (Magnusson et al., 1995), ac susceptibility (Nordblad et al., 1998) and magnetic aging (Svedlindh et al., 1999).

A controversial point to this model arises from similar results obtained in Nb samples, because some authors (Sigrist & Rice, 1995) attribute that π junctions are a consequence of the *d*-wave pairing symmetry, which is nonexistent in this system. The PME observed in Nb (Thompson et al., 1996; Minhaj et al., 1994; Kostic et al., 1996) and Nb thin films (Ortiz et al., 2001; Terentiev et al., 1999) was demonstrated to be strongly influenced by the sample geometry and surface. In some cases, the polishing of the surfaces affects the PME significantly, leading to its disappearance. **Fig. 7** shows the magnetization results of a Nb disk before and after polishing the sample surface, where it is possible to see that the PME disappears after the sample is polished. A surface dependent PME in $YBa_2Cu_3O_{7-x}$ single crystals was also found (Lucht et al., 1995).

These results motivated the proposal of mechanisms to explain the PME without taking into account effects from intrinsically nonconventional superconductivity, and models based on flux trapping and flux compression effects were proposed. According to these models, a nonequilibrium compressed flux state may be generated and stabilized by inhomogeneous cooling of the sample, so that its surface becomes superconducting prior to the bulk (Koshelev & Larkin, 1995). Then, the magnetic flux may be pushed into the sample, creating a flux compressed state upon further cooling.

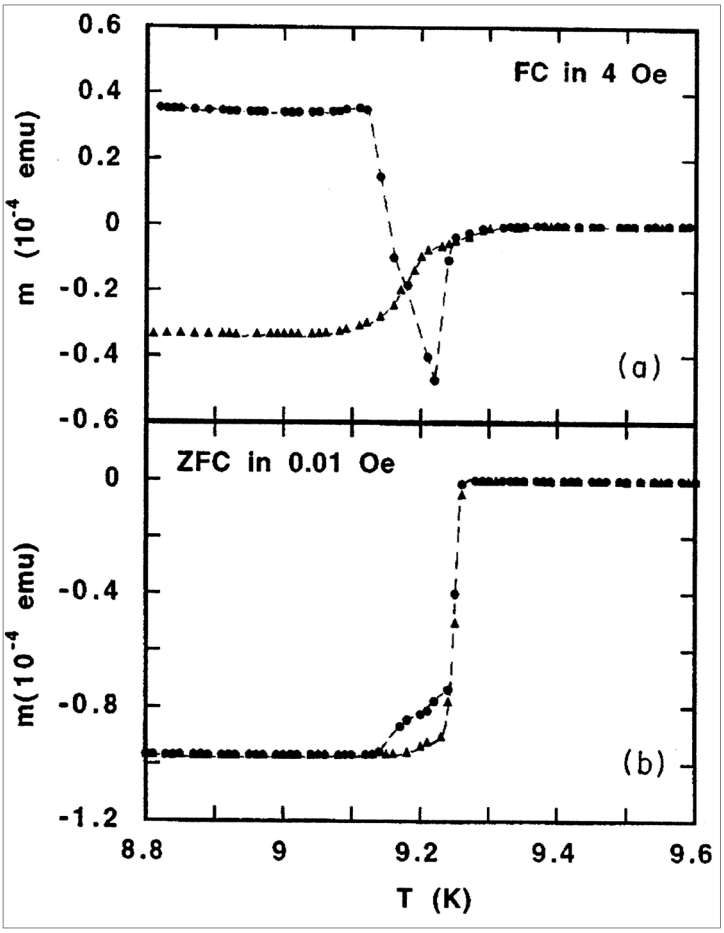

Fig. 7. FC (a) and ZFC (b) experiments in a Nb disk. The circles were taken before polishing the sample surface, and the triangles were taken after polishing the sample surface. In this case, the polishing of the surface affects the PME, leading to its disappearance. From Kostic´ et al., 1996.

Similarly, the formation of a giant vortex state on the sample surface proposed by Moshchalkov et al. (Moshchalkov et al., 1997) may produce a compression of the trapped flux. According to the authors, the PME observed in high-T_C and Nb superconducting samples can be explained by the persistence of a giant vortex state with a fixed orbital quantum number *L*, formed during the FC regime at the third critical field. However, the amplitude of the PME is suppressed by applying a magnetic field. The giant vortex state was also shown to be responsible for PME in small disks of Al samples (Geim et al., 1998), where transitions between metastable giant vortex states having different angular momenta (*L*) have been observed. The transitions compress the giant vortex into smaller volumes, allowing extra flux to penetrate in the sample surface and producing the paramagnetic moments.

The flux capture by samples with a special shape proposed by Obukhov (Obukhov et al., 1998), may also produce compression of the trapped flux. According to the author, an unusual behavior of the long-time relaxation of the magnetization after a FC procedure may show not only an increase in the magnetization over the time but a change of sign from negative to positive. This interesting result was observed in melt-textured $YBa_2Cu_3O_{7-x}$ samples (Pureur et al., 2001), as shown by the inset in the **Fig. 5**.

A model to explain the PME observed in Josephson-junctions arrays, such as Nb-Al_2O_3-Nb (Nielsen et al., 2000), was proposed to account for the paramagnetism without invoking the role of π junctions or *d*-wave superconductivity (Araujo-Moreira, 1997; Barbara, 1999; Nielsen et al., 2000). According to this model, the screening of the array of these multiply-connected superconductors is provided by the loops at its boundaries, and the diamagnetic currents running at the external perimeter induce currents in the opposite sense inside the array. These inner currents generate a paramagnetic scenario under certain conditions. This mechanism is shown in **Fig. 8**.

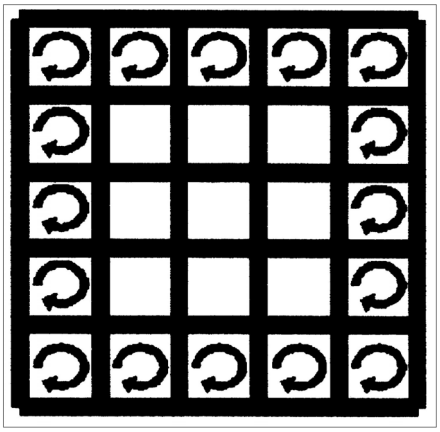

Fig. 8. Mechanism for generation of a paramagnetic current inside a multiply-connected superconducting sample. From Nielsen et al., 2000.

According to this model, only the exterior plaquettes create a diamagnetic screening current on the outside of the sample, and as a consequence a paramagnetic current of the same magnitude is created inside the sample. Simulations taking into account the mutual-inductance interactions between loops in the array confirm that PME might be the dominant response, depending on the field strength and parameters as the self-inductance and capacitance of the Josephson junctions (Rotoli et al., 2001).

The granularity in superconductors emulates a disordered network of Josephson junctions, and the paramagnetic moments observed in granular thin films of Nb and $YBa_2Cu_3O_{7-x}$ has also been described as an intrinsic effect of multiply-connected superconductors.

Important results were obtained by Kusmartsev et al. (Kusmartsev et al., 1997) after cooling large $YBa_2Cu_3O_{7-x}$ single crystals in strong applied fields. The authors called this phenomenon the high-field paramagnetic effect (HFPME) so that it may be distinguished

from the low-field PME. The HFPME was found to depend on the cooling rate and the sample size, which suggests that the paramagnetic moment in this case might be induced by a flux compression mechanism. The **Fig. 4** shows representative results obtained by Kusmartsev et al.

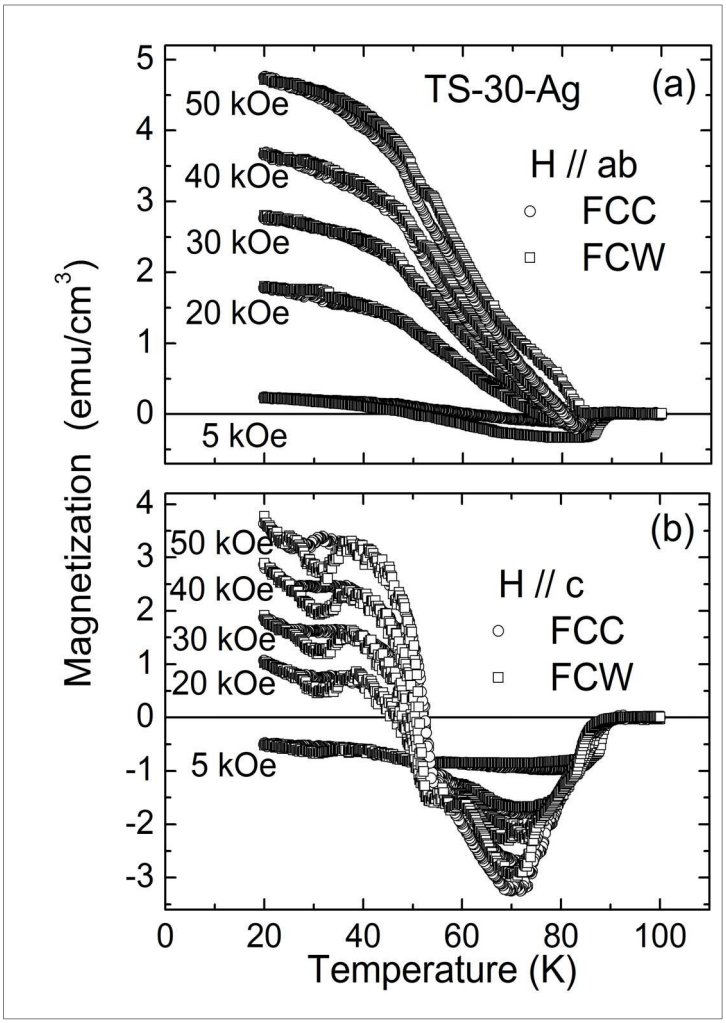

Fig. 9. FCC and FCW magnetizations in a melt-textured $YBa_2Cu_3O_{7-x}$ sample exhibiting a strong PME. From Dias et al., 2004.

The PME at high magnetic fields was also observed by Dias et al. (Dias et al., 2004) in different melt-textured $YBa_2Cu_3O_{7-x}$ samples containing large amounts of the Y_2BaCuO_5 (Y-211) phase. Magnetic fields up to 50 kOe were applied either parallel or perpendicular to the *ab* planes and the magnitude of the high-field paramagnetic moment increases when the

field is augmented. The **Fig. 9** shows FCC and FCW magnetizations as a function of the temperature in a melt-textured $YBa_2Cu_3O_{7-x}$ sample measured in the indicated fields applied parallel and perpendicular to the *ab* planes. In the **Fig. 9a** the data are obtained when the field is applied parallel to the *ab* plane. These results present the general trends of the PME shown by the melt-textured YBaCuO samples. In the **Fig. 9b** are depicted the peculiar results obtained when the field is applied along the *c*-axis. In this case the positive contribution to the moment rises abruptly at an almost field-independent temperature around 55 K, then shows a tendency to saturate at low temperatures at values varying roughly proportional to the applied field. When the magnetic field increases the magnetization also increases and for magnetic fields below 5 kOe the magnetization is negative, as shown in the **Fig 9b**.

The effect shows a strong and anomalous relaxation, such that the paramagnetic moment increases as a function of the time, as shown in **Fig. 10**.

According to the authors, the pinning by the Y-211 particles is relevant and the formation of a flux-compressed scenario modulated by pinning and a strong flux-creep is a possible origin of the observed PME. Recently, the high-field PME was also observed in an $Y_{0.98}Ca_{0.02}Ba_2Cu_3O_{7-x}$ single crystal (Dias et al., 2010), and the results were attributed to strong flux compression state into the sample modulated by pinning. An important review of the paramagnetic Meissner effect and related dynamical phenomena was presented by M.S. Li (Li, 2003), with emphasis on the theoretical description of the π junctions.

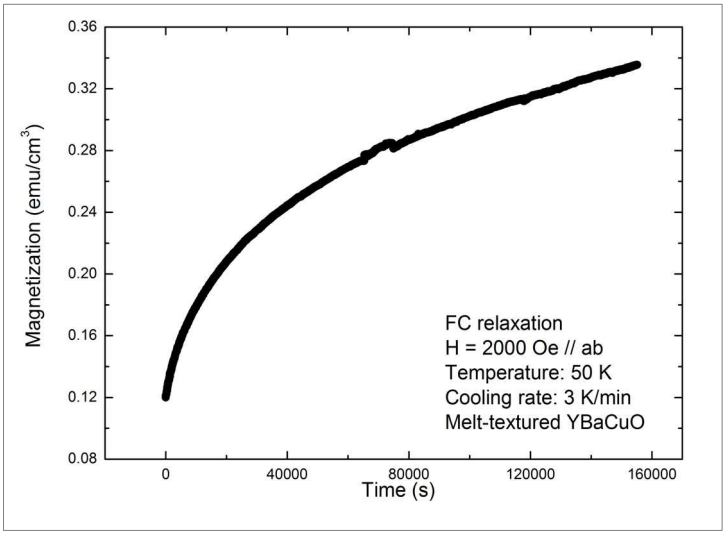

Fig. 10. Strong time dependence of the FCC magnetization in a melt-textured $YBa_2Cu_3O_{7-x}$ sample exhibiting the PME.

1.2 Mechanical properties of YBCO-bulk materials

1.2.1 Theoretical fundamentals

Indentation testing is a simple method that consists essentially of touching the material of interest, whose mechanical properties such as elastic modulus and hardness are unknown, with another material whose properties are known (Fischer-Cripps et al., 2004). The technique has its origins in Mohs' hardness scale of 1822, in which materials that are able to leave a permanent scratch in another were ranked as harder materials, with diamond assigned the maximum value of 10 on the scale. The establishment of the Brinell, Knoop, Vickers and Rockwell tests all follow from a refinement of the method of indentation test, in which the length scale of the penetration is measured in nanometers rather than microns or millimeters, the latter being common in conventional hardness tests. Apart from the displacement scale involved, the distinguishing feature of most nanoindentation testing is the indirect measurement of the contact area.

In conventional hardness tests, the area of contact is calculated from direct measurements of the dimensions of the residual impression in the specimen surface upon the removal of load. In nanoindentation tests, the size of the residual impression is of the order of microns and too small to be conveniently directly measured. Thus, it is usual to determine the area of contact by measuring the depth of indentation of the indenter into the specimen of interest. This, together with the known geometry of the indenter, provides an indirect measurement of the contact area at full load. For this reason, nanoindentation can be considered a special case of depth-sensing indentation or instrumented indentation testing.

In this section, we would like to do a brief explanation of the different hardness tests employed to characterize the $YBa_2Cu_3O_{7-x}$ samples textured by Bridgman and TSMG technique. Concretely, we will explain in detail the micro-, nano- and even picoindentation, according to the characteristic indentation sizes that fall into a particular size range and the applied load employed.

1.2.1.1 Microindentation

The purpose of microindentation hardness testing is to study fine scale changes in hardness. This technique is also commonly called microhardness testing, although this term is misleading because it implies that the hardness is extremely low. The Vickers and the Knoop tests, which are the two most common microindentation tests, will be described in more detail in the present section.

The term microhardness test usually refers to static indentations made with loads not exceeding 1kgf. The indenter is either the Vickers diamond pyramid or the Knoop elongated diamond pyramid. The surface being tested generally requires a metallographic finishing; the smaller the load used, the higher the surface finish required.

The Knoop indenter is a diamond ground to pyramidal form that produces a diamond shaped indentation, having an approximate ratio between long and short diagonals of 7:1. The depth of indentation is about 1/30 of its length. The Knoop hardness number (*KHN*) is the ratio of the load applied to the indenter to the unrecovered projected area as:

$$KHN = \frac{F}{A} = \frac{P}{CL^2} \tag{1}$$

Where F or P is the applied load in *kgf*, A is the unrecovered projected area of the indentation in mm^2, L is the measured length of the long diagonal of indentation in *mm*, and C is a constant of the indenter relating the projected area of the indentation to the square of the length of the long diagonal, and equal to 0.07028.

The Vickers diamond pyramidal indenter is ground in the form of a square pyramid with an angle of 136° between faces. The depth of indentation is about 1/7 of the diagonal length. The Vickers diamond pyramid hardness number (HV) can be obtained by using the following equation:

$$HV = \frac{2\mathrm{F}\sin\frac{136°}{2}}{d^2} \quad or \quad HV \approx 1.854\frac{F}{d^2} \tag{2}$$

Where F is the load in *kgf*, d is the arithmetic mean of the two diagonals, d_1 and d_2 in *mm* and HV is the Vickers hardness.

Comparing the indentations made with Knoop and Vickers diamond pyramid indenters for a given load and test material we can conclude:

- Vickers indenter penetrates about twice as deep as Knoop indenter
- Vickers indentation diagonal about 1/3 of the length of Knoop major diagonal
- Vickers test is less sensitive to measurement errors than Knoop test
- Vickers test is more sensitive to measurement errors than Knoop test
- Vickers test is best for small rounded areas
- Knoop test is best for small elongated areas
- Knoop test is good for very hard brittle materials and very thin sections

1.2.1.2 Nanoindentation

During the last years, Instrumented Indentation Testing has been widely employed. Also known as depth-sensing indentation, continuous-recording indentation, ultra-low load indentation or nanoindentation, ITT is a relatively new form of mechanical testing, which significantly expands the capabilities of traditional hardness tests at macro- and microscale. It employs high-resolution instrumentation to continuously control and monitor the loads and displacements of an indenter (Golovin et al., 2008; Pharr et al., 1992). This technique presents several advantages compared to the microindentation technique:

- It is a local probe that can evaluate the properties of a material in different areas.
- It is depth-sensing, so it can characterize a material at different depths, unlike most scanning probe techniques, which usually only work at a given indentation depth.
- It can also measure the Elastic modulus (E) of the material.

Moreover, this technique is especially well suited for the characterization of small volumes of material, such as single grains or phases in a composite (Roa et al., 2007), dislocation dynamics (Gaillard et al., 2006), small structures (Choi et al., 2003) or thin films and coatings (Gaillard et al., 2008; Beegan et al., 2005; Roa et al., 2009a, 2011a; Rayon et al., 2011).

Finally, this technique eliminates the need to visualize the imprints produced during the test for homogeneous materials, which makes the extraction of mechanical properties easier. Due to all these advantages, nanoindentation could be a good and versatile technique for characterizing the mechanical properties of a given component.

The nanoindenter is an equipment which measures load and maximum indentation depth as a function of time during loading and unloading, and displays load-displacement data. Depending on the details of the specific testing systems, loads as small as 1 nN can be applied, and displacements of 0.1 nm can be measured. Stress-strain curves (σ–ε) and mechanical properties such as hardness (H), elastic modulus (E), fracture toughness (K_{IC}), yield strength (σ_{ys}), or shear stress (τ), can be obtained from the P-h data and with the corresponding tip indenter. The different indenters can be classified in four different groups:

i. *Pyramidal:* the most used sharp indenter is the Berkovich. It is a three-sided pyramid with the same depth-to-area relation as the four sided Vickers pyramid commonly used in microhardness. This indenter allows obtaining the H and E. The K_{IC} of brittle materials can also be determined with this indenter without high accuracy.
ii. *Spherical:* for this kind of indenters, the contact stress is initially small and produces only elastic deformation. As the spherical indenter is driven into the surface, a transition from elastic-to-plastic deformation occurs, which can theoretically be used to examine the σ_{ys} and obtain the σ–ε curve (Field et al., 1993).
iii. *Cube-corner:* a three-sided pyramid with mutually perpendicular faces arranged in geometry like the corner of a cube. The center-line-to-face angle for this indenter is 34.3°. The sharper cube-corner indenter produces much higher stress and strain in the vicinity of the contact, which is useful, for example, in producing very small and well defined cracks at the corners of the residual imprints in brittle materials.
iv. *Conical indenters:* this type of indenter is interesting due to the existence of stress concentrations at the sharp edges of the indenter. It is difficult to manufacture conical diamonds with sharp tips, making them of little use in nanoindentation technique (Tsui et al., 1997).

Moreover, in order to obtain reproducible results, several factors should be controlled during the indentation tests:

- *Choosing an appropriate indenter:* this is one of the most important steps and requires the consideration of a number of factors. One of them is the strain the tip imposes on the test materials. Although the indentation process produces a complex strain field beneath the indenter, it has been proven to be useful to quantify this field with a single quantity, often termed as the characteristic strain. There are problems, however, in obtaining accurate measurements of H and E with cube-corner indenters (Hay et al., 1999). Although not entirely understood, the problems appear to have two separate origins: first, as the angle of the indenter decreases, friction in the specimen-indenter interphase and its influence on the contact mechanics becomes increasingly important; on the other hand, to obtain the relation between the contact stiffness (S), contact area ($A(h_c)$) and effective elastic modulus (E_{eff}), corrections are required, and the magnitude of the correction factor depends on the angle of the indenter.
- *Environmental control:* to take full advantage of the fine displacement resolution available in most ITT systems, several precautions must be taken when choosing and

preparing the testing environment. Uncertainties and mistakes in measured displacement arise from two separate environmental sources: vibration and temperature. To reduce vibration, the nanoindenter should be located on quite, solid foundation and mounted on vibration-isolation system. Thermal stability can be provided by closing the apparatus in a thermally buffered cabin and controlling the room temperature to within ± 0.5°C.

- *Surface preparation:* one of the most important factors is the surface roughness of the samples, which is extremely important during the nanoindentation test because the mechanical properties are obtained from contact areas, which are calculated from the contact depth and area function. The main problems are found when the characteristic wavelength of the roughness is comparable to the contact diameter.
- *Testing procedure:* to avoid interference from previous assays, and ensure the independence of the measurement, successive indentations should be separated up to 20-30 times the maximum indentation depth (h_{max}) when Berkovich or Vickers indenters are employed. However, for other geometries, the rule is to perform indentations separated from 7 to 10 times the maximum contact radius.
- *Detecting the surface:* the most important step of any good nanoindentation test procedure is to accurate identificate the location of the specimen's surface. For hard and stiff materials, such as hardened metals and ceramics, the load and/or contact stiffness, both of which increase upon contact, are often employed. However, for soft compliant materials (like polymers and biological tissues), the rate of increase in load and contact stiffness is often too small to allow for accurate surface identification. In these situations, a better method is sometimes offered by dynamic stiffness measurement (Pethica et al., 1989; Lucas et al., 1998).

a. Hardness and Elastic modulus determination

In this section we will explain the method developed by Oliver and Pharr (Pharr et al., 1992; Oliver et al., 1992) to determine the hardness (H) and the elastic modulus (E) from the unloading part of recorded indentation load/unload (or P-h curves, such as **Fig. 11**).

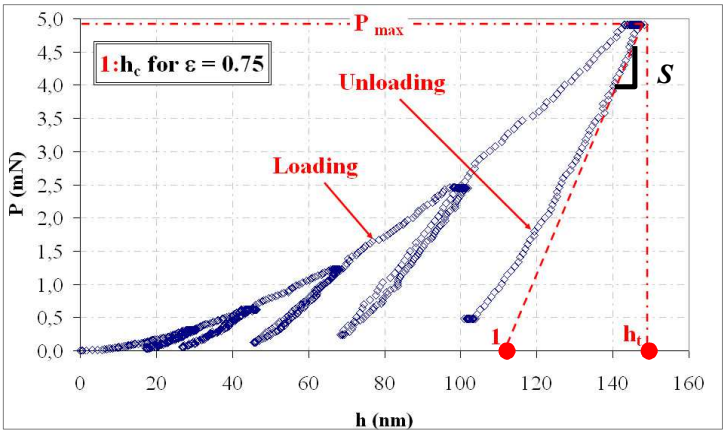

Fig. 11. Schematic representation of indentation P-h curve showing important measured parameters (From Roa et al., 2007).

The H is calculated by dividing the load by the projected contact area ($A(h_c)$) at maximum applied load, P_{max}:

$$H = \frac{P_{\max}}{A(h_c)} \tag{3}$$

where the contact depth (h_c) is determined as:

$$h_c = h_{\max} - \varepsilon \frac{P_{\max}}{S} \tag{4}$$

being h_{max} the maximum indentation depth, ε a parameter approximately equal to 0.75 for a Berkovich tip indenter, and S the unloading contact stiffness at maximum indentation depth (dP/dh, see **Fig. 11**). In the case of a perfect Berkovich tip, the $A(h_c)$ is determined as:

$$A(h_c) = 24.56 h_c^2 \tag{5}$$

However, in practice the projected contact area differs from this value when the tip is worn out, because the different angles of the faces may be somehow different from the nominal. Hence, the projected contact area must be regularly calibrated. When catastrophic fracture mechanisms occur, the $A(h_c)$ obtained by this theoretical method is overestimated, and results in an H underestimation. To avoid this problem, the real contact area should be determined using a technique of microscopy (as Scanning Electron Microscopy or Atomic Force Microscopy) and the contact area must be recalculated in order to avoid the sink-in or pile-up effects for brittle and/or ductile materials, respectively (Roa et al., 2009d, 2010c, 2011b).

The effective elastic modulus (E_{eff}) has been expressed in terms of S and $A(h_c)$ as:

$$E_{eff} = \frac{1}{\beta} \frac{\sqrt{\pi}}{2} \frac{S}{\sqrt{A(h_c)}} \tag{6}$$

where β is a geometrical factor (1.034). This parameter takes into account the lack of symmetry of the Berkovich indenter. Then, according to the Oliver and Pharr approach (Oliver et al., 1992), the Elastic modulus can be obtained as:

$$\frac{1}{E_{eff}} = \frac{1-\nu^2}{E} + \frac{1-\nu_i^2}{E_i} \tag{7}$$

where E and υ are the Elastic modulus and the Poisson's ratio ($\nu_{YBa2Cu3O7-x}$ = 0.3 (Roa et al, 2007, 2009d, 2010a, 2010c, 2011b, 2011d), respectively. The subindex i denotes the indenter properties (E_i = 1141GPa and $\upsilon_i = 0.07$) (Oliver et al., 1992; Pharr et al., 1992).

b. Fracture toughness

Moreover, nanoindentation provides information about contact mechanisms taking place in the material. In brittle materials indented with a Berkovich tip, surface examination of residual imprints has revealed the appearance of several typical features: surface deformation effects such as *sink-in* (Johnson et al., 1985; Alcala et al., 2000), microcracks or damage inside the

imprints (Burghard et al., 2004); and fracture mechanisms such as *radial cracks* emanating from the imprint corners (Roa et al., 2008a, 2008b), and *chipping* (Lawn et al., 1975).

The resistance of the material against crack propagation, characterised by the fracture toughness K_{IC} (Anderson et al., 2005), is a critical mechanical parameter in brittle materials. Fracture toughness estimation by microfracture Vickers indentation is a well-known and broadly employed technique in ceramic materials. Usually, a Vickers diamond pyramid indenter at loads greater than 1 N is used to nucleate radial cracks at the imprint corners. The cracks emanating from the corners of a Vickers or Berkovich indenter are arrested when the residual stress driving force at the crack tip is in equilibrium with the K_{IC}. Several expressions are widely employed to extract the fracture toughness, depending on the indenter geometry and crack morphology. In this experimental work, the method we are pursuing is based on the radial cracking which occurs when brittle materials are indented by sharp indenter such as Vickers or Berkovich diamond (Casellas et al., 2007; Jang et al., 2008). K_{IC} is then evaluated using the equation developed by Lawn, Evans, and Marshall (Lawn et al., 1980):

$$K_{IC} = a\left(\frac{E}{H}\right)^{1/2}\left(\frac{P}{c^{32}}\right) \tag{8}$$

where α is an empirical constant depending on the indenter geometry (α=0.016 for pyramidal tips), P is the peak indentation load, c is the length of the radial cracks, E is the elastic modulus, and H is the hardness value. The fracture toughness of $YBa_2Cu_3O_{7-x}$ melt-textured samples has been determined by Vickers indentation (Leblond-Harnois et al., 2000; Li et al., 1997; Yoshino et al., 2001; Leenders et al., 1999; Cook et al., 1987; Fujimoto et al., 1992), and also by the single-edge notch beam (Joo et al., 1998) and bending (Giese et al., 1990) techniques. Values in the range of K_{IC}=0.4-2.8 MPa·m$^{1/2}$ have been found, with a scattering attributed to differences between the techniques employed to obtain this parameter. In addition, K_{IC} is influenced by exact matrix composition. For instance, Joo *et al.* (Joo et al., 1998), reported that the fracture toughness of $YBa_2Cu_3O_{7-x}$ increased from K_{IC}=1.60 MPa·m$^{1/2}$ to 2.80 MPa·m$^{1/2}$ by adding a 15% in volume of silver to the matrix.

c. Yield strength and stress-strain curve

The stress and deflection arising from the contact between two elastic solids are of particular interest to understand the first steps of indentation testing. The contact depth between a rigid sphere and a flat surface for small indentation depths was described by Hertz (Hertz et al., 1881). This phenomenon is shown in **Fig. 12**. The radius of the circle of contact is a, the total indentation depth is h_{max}, the depth of the circle of contact from the specimen free surface is h_a, and h_p is the distance from the bottom of the contact to the contact circle.

When using spherical tips, the contact point is more difficult to be determined, due to the moderate increase in stiffness during the initial contact, and the interaction between the tip and samples before contacting. The indentation load-displacement data were analyzed based on the Hertz equation in the elastic region as follows (Oliver et al., 2004; Field et al., 1993; Field et al., 1995):

$$P = \frac{3}{4}E_{eff}\sqrt{R}\sqrt[3/2]{h_e} \tag{9}$$

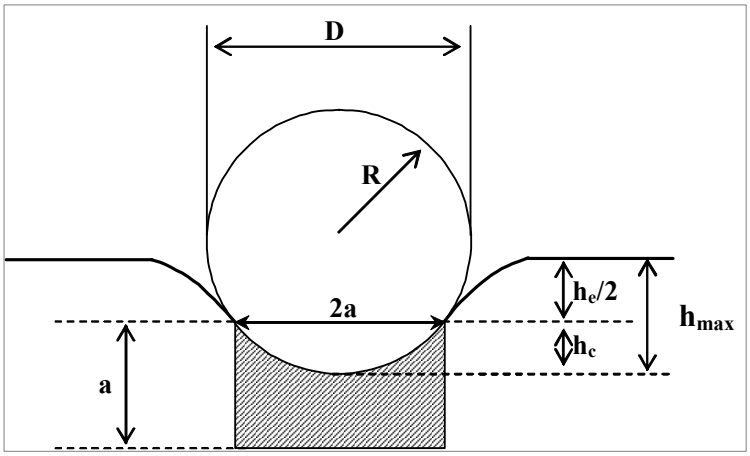

Fig. 12. Schematic representation of spherical indentation (From Roa et al., 2010b).

where h_e is the elastic indentation depth. Recently, Barsoum *et al.* (Moseson et al., 2008) proposed the fitting of the stiffness vs. indentation depth data, and extrapolating to zero, as predicated by a relation between E_{eff} and a, as follows (Roa et al., 2010b, 2010c, 2011b):

$$S = 2E_{eff}a \tag{10}$$

Hertz found that the radius of the circle of contact, a, is related to the indentation load, P, the indenter radius, R, and the elastic properties for small indentation depths of the material by:

$$j = \sqrt[3]{\frac{3}{4}\frac{PR}{E_{eff}}} = \sqrt[3]{\frac{3}{4}\frac{PR}{\frac{1}{\beta}\frac{\sqrt{\pi}}{2}\frac{S}{\sqrt{A(h_c)}}}} \tag{11}$$

The mean contact pressure, p_m, between the indenter and the material is the applied load divided by the contact area. For small indentation depths, it can be obtained from the Hertzian equations as:

$$p_m = \frac{P}{\pi a^2} = \frac{4E_{eff}}{3\pi}\left(\frac{a}{R}\right) \tag{12}$$

The mean contact pressure is referred to as the "*indentation stress*" and the quantity *a/R* as the "*indentation strain*". This equation allows us to plot the stress-strain curves when we use a spherical tip. The left side of this equation represents the indentation stress or mean contact pressure, also referred to as the Meyer hardness (Basu et al., 2006). The expression in parentheses on the right side of this equation represents the indentation strain (Rayon et al., 2011).

The maximum tensile stress occurs at the edge of the contact circle in the surface and can be expressed as (Fischer-Cripps, 1999):

$$\sigma_{\max} = \frac{1}{2}(1-2\nu)p_m \tag{13}$$

The yield stress of the material, σ_{ys}, can be obtained using the following expression:

$$p_m = 1.1\sigma_{ys} \tag{14}$$

This parameter will give information about the transition from elastic to elastic-to-plastic response (Jiménez-Piqué et al., 2007). The maximum shear stress (τ_{max}) is produced beneath the indentation axis at a depth close to *0.5a*, and equal to:

$$\tau_{\max} = 0.46p_m \tag{15}$$

The maximum shear stress is also known as the Tresca criterion. This assumes that yield occurs when the shear stress τ exceeds the shear yield strength, τ_{ys} (Tsui et al., 1997; Roa et al., 2008a):

$$\tau = \frac{\sigma_1 - \sigma_3}{2} \leq \tau_{ys} \tag{16}$$

Where σ_1 and σ_3 are the principal stresses (also, can be re-written as σ_x and σ_z, respectively).

1.2.1.3 Picoindentation

The applied load in this case is much lower than in the previous one. Normally, this technique produces some indentations of few nanometers (generally fully elastic) obtaining the Elastic modulus. Picoindentation by means of atomic force microscopy-force spectroscopy (AFM-FS) presents several advantages over standard methods with regard to the quantification of *E* values:

- First, the measurements are extremely local (small contact areas between the sample and the probe, of few nm^2) and can be performed on different areas so as to average the mechanical properties of the samples.
- Second, it is a form of depth-sensing, so it allows characterization of a material at different indentation depths without surpassing the yield strength (fully elastic regimen).
- Finally, it is not necessary to visualize and characterize the imprint produced during the indentation test, which simplifies the calculation in order to extract the *E* values.

These advantages mean that picoindentation is a suitable and reliable technique for measuring E values while applying loads ranging from a few nN down to the pN level. The study of force versus displacement (F-z) curves can shed new light on the elastic properties of hard materials, as these curves are similar to those obtained with classic microscopic or nanoscopic indentation tests.

The different steps of the method to extract the elastic modulus value using the AFM-FS and Hertz equations are described below (Roa et al., 2011e, 2011f):

1. **Cleaning the tip:** it is important to remove contaminants covering the tip. First, rinse the tip with miliQ water, acetone and ethanol and dry it under a nitrogen flow. After that, put the tip in an ozone cleaning chamber during 30-35 minutes, and ultraviolet light.
2. **Measuring the tip radius by means of a NiO Pattern:** A NiO sample that features extremely sharp crystallographic ridges is used for measuring the tip radius. Then, as the sample ridges are nominally sharper than the tip apex, it is possible to obtain a "tip image" using blond reconstruction software. AFM images of the pattern should be collected in tapping mode with scan of 0.5µm by 0.5µm, scan rates of 1 Hz and 512 by 512 pixels. The blind reconstruction software employed is Scanning Probe Image Processor, see **Fig. 13** (Roa et al., 2011e).

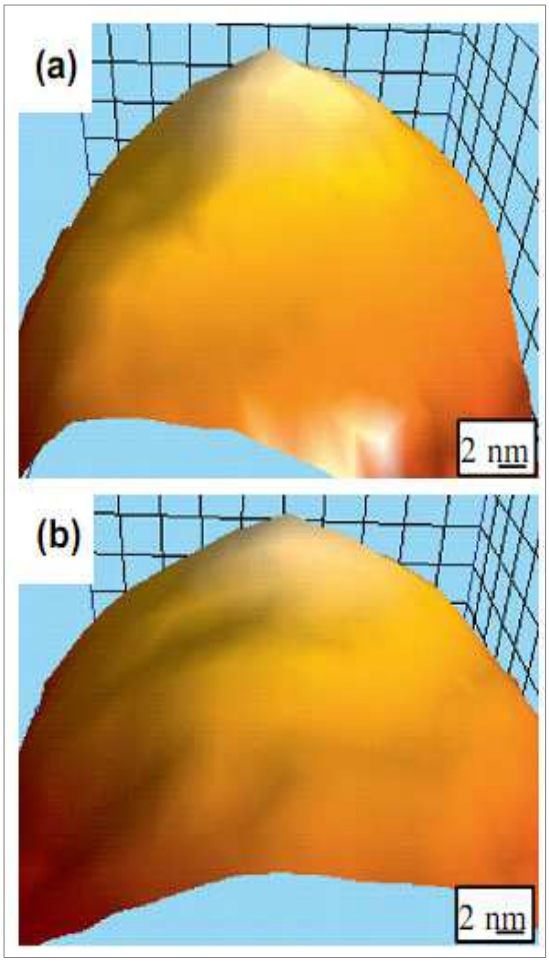

Fig. 13. Software reconstruction images of the AFM tip, (a) before the picoindentation test, and (b) after the picoindentation test. From Roa et al., 2011e.

3. **Indentation process:** after that, an image of the sample should be taken, and several spots (at least 40 spots) should be chosen in order to perform one indentation per spot, see **Fig. 14a** (from Roa et al., 2011e).

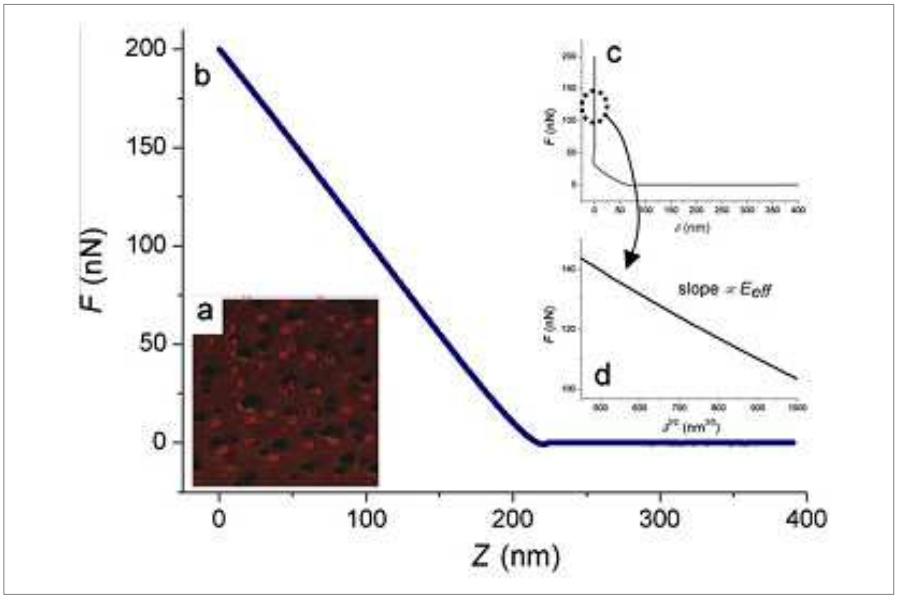

Fig. 14. Images of the different steps taking place during the picoindentation process. (a) AFM image with 40 different spots. (b) F vs. z cantilever deflection. (c) F vs δ, and (d) F vs. $\delta^{3/2}$ from the slope of Elastic modulus, which is calculated using Hertzian equations. From Roa et al., 2011e.

F is calculated as (see **Fig. 14b**):

$$F = k_v \Delta z \tag{17}$$

where Δz is the cantilever deflection, defined as:

$$\Delta z = \frac{\Delta V}{S} \tag{18}$$

where ΔV is the increment in photodetector vertical signal, as the tip comes into contact with the sample, and S is the sensitivity, which is the slope of the contact region of a force curve performed on a rigid sample.

The indentation depth (δ) due to F is calculated as (see **Fig. 14c**):

$$\delta = z - \Delta z \tag{19}$$

where z represents the piezo-scanner displacement along the axis perpendicular to the sample plane. After puncturing the sample, a topographic image should be captured in

order to ensure that the sample had not undergone any plastic deformation. Only *F-z* curves that presented negligible lateral deflection should be considered to extract the mechanical response. *F-z* curves obtained at a certain *F* value were analyzed using the Hertz model in the elastic region (Oliver et al., 2004; Field et al., 1993, Field et al., 1995) by means of equation 20 (see F**ig. 14d**):

$$F = \left(\frac{3}{4} E_{eff} \sqrt{R}\right) \delta^{3/2} \tag{20}$$

where E_{eff} can be obtained using the equation 7. In this case the subindex *i* corresponds to the mechanical properties of the AFM probe (SiO_2 with E = 76 GPa, and υ_i = 0.17 (Oliver et al., 1992)). The quality of *S* value relies on the absence of elastic deformation of the reference sample.

1.2.2 State of the art

The mechanical properties of $YBa_2Cu_3O_{7-x}$ (Y-123 or YBCO) samples have been studied during the last years. The most important properties studied have been the elastic modulus, *E*, the hardness, *H* (*at micro-/ nanometric scale*), the toughness fracture, K_{IC}, and the yield stress value, σ_{ys}. Some authors studied the mechanical properties at room or at cryogenic temperatures, also known as work temperature (T_w). Lots of different techniques could be used to determine these parameters. The reported values of *E*, *H*, K_{IC} and σ_{ys} of $YBa_2Cu_3O_{7-x}$ samples (bulk materials) obtained using indentation techniques (macro-, micro-, nano- and/or picoindentation techniques) are summarized in *table 1, 2, 3 and 4*, respectively.

Author	Material	E (GPa)	Method	Year
Lucas et al.	$YBa_2Cu_3O_{7-x}$	154.30 ± 16.34	Indentation	1996
Güçlü et al.	Polycrystalline, 50K	47.20	Vickers indentation	2005
	Polycrystalline, 160K	29.63		
	Polycrystalline, 180K	28.47		
	Polycrystalline, 293K	9.39		
Goyal et al.	Y_2BaCuO_5 (Y-211)	213	Nanoindentation	1991
	Texturized	182	Nanoindentation	1991
Roa et al.	Y-123[1] at 5mN	197 ± 7	Nanoindentation	2007
	Y-211[1] at 5mN	194 ± 9		
	Y-123/Y-211[1] at 5mN	201 ± 7		
	Y-123[1] at 10mN	189 ± 4		
	Y-211[1] at 10 mN	206 ± 4		
	Y-123/Y-211[1] at 10mN	204 ± 6		
	Y-123/Y-211[1] at 30mN	180 ± 5		
	Y-123/Y-211[1] at 100mN	173 ± 3		

Table 1. Literature values of *E* for $YBa_2Cu_3O_{7-x}$ obtained by indentation techniques.

[1] *Texture process:* Bridgman technique

Author	Material	E (GPa)	Method	Year
Foerster et al.	YBCO-TSMG (*ab*-plane)	177 ± 10[2]	Nanoindentation	2008
	YBCO-TSMG + 5% Ag_2O (*ab*-plane)	220		
	YBCO-TSMG + 10% Ag_2O (*ab*-plane)	149 ± 4		
	YBCO-TSMG + 15% Ag_2O (*ab*-plane)	≅ 150		
	YBCO-TSMG (*ca(b)*-plane)	177 ± 10[2]		
	YBCO-TSMG + 5% Ag_2O (*ca(b)*-plane)	≅ 175		
	YBCO-TSMG + 10% Ag_2O (*ca(b)*-plane)	≅ 175		
	YBCO-TSMG + 15% Ag_2O (*ca(b)*-plane)	≅ 150		
Roa et al.	Y-123[3] at 5mN	176 ± 15	Nanoindentation	2009d
	Y-211[3] at 5mN	224 ± 18		
	Y-123/Y-211[3] at 5mN	208 ± 21		
	Y-123[3] at 10mN	174 ± 17		
	Y-211[3] at 10 mN	207 ± 11		
	Y-123/Y-211[3] at 10mN	190 ± 16		
	Y-123/Y-211[3] at 30mN	140 ± 14		
	Y-123/Y-211[3] at 100mN	129 ± 6		
Roa et al.	$YBa_{1.75}Sr_{0.25}Cu_3O_{7-\square}$	106 ± 4	FS[4]-AFM	2009b
Roa et al	Y-123/Y-211-Bridgman	123.5 ± 3.4	Nanoindentation	2010b,c
Bartolomé et al.	YBCO-TSMG	120 ± 5	Nanoindentation	2010a
Roa et al.	YBCO-Bridgman	128 ± 5	Nanoindentation	2011b,d
Roa et al.	Y-123 at 300K (tetragonal, T) [3]	185 ± 7	FS*-AFM	2011c
	Y-211 at 300K (T) [3]	202 ± 5		
	Y-123 at 300K (orthorhombic, O) [3]	189 ± 4		
	Y-211 at 300K (O) [3]	201 ± 6		
	Y-123 at 300K (T) [3]	192 ± 3		
	Y-211 at 300K (T) [3]	208 ± 7		
	Y-123 at 300K (O) [3]	193 ± 4		
	Y-211 at 300K (O) [3]	205 ± 5		
	Y-123 at 300K (T)[5]	179 ± 4		
	Y-123 at 300K (O)[5]	182 ± 5		
	$YBa_{1.75}Sr_{0.25}Cu_3O_{7-x}$[5]	106 ± 4		
	$Y_{0.98}Ca_{0.02}Ba_2Cu_3O_{7-x}$[5]	100 ± 4		

Table 1. Literature values of E for $YBa_2Cu_3O_{7-x}$ obtained by indentation techniques (continuation).

[2]At maximum indentation depth (around *1300nm*)
[3] *Texture process:* TSMG technique
[4] *FS:* Force Spectroscopy
[5] *Texture process:* Self-flux technique

Author	Material	H (GPa)	Method	Year
Cook et al.	YBCO	8.7	Vickers Indentation	1987
Goyal et al.	Textures	6.7	Vickers Indentation	1992
		10.8	Nanoindentation	
Goyal et al.	Y-211	14.0	Nanoindentation	1992
Lucas et al.	Y-123	10.28 ± 1.67	Indentation	1996
Li et al.	MTG-1100ºC, 5min	5.4	Vickers indentation	1997
	MTG-1100ºC, 10min	11.0		
	MTG-1100ºC, 15min	10.3		
	Solid State reaction	10.3		
Lim et al.	Single crystal	7.81 ± 0.23	Nanoindentation	2001
Yoshimo et al.	YBCO 40K	18 ± 2.5	Vickers Indentation	2001
	YBCO 293K	5.2 ± 0.5		
Güçlü et al.	Polycrystalline, 50K	3.58	Vickers Indentation	2005
	Polycrystalline, 160K	1.03		
	Polycrystalline, 180K	0.95		
	Polycrystalline, 293K	0.53		
Roa et al.	Y-123[6] at 5mN (O)	10.4 ± 0.5	Nanoindentation (Berkovich)	2007
	Y-211[6] at 5mN (O)	19.1 ± 0.8		
	Y-123/Y-211[6] at 5mN (O)	14.8 ± 0.5		
	Y-123[6] at 10mN (O)	11.2 ± 0.4		
	Y-211[6] at 10 mN (O)	16.9 ± 0.6		
	Y-123/Y-211[6] at 10mN (O)	15.1 ± 0.3		
	Y-123/Y-211[6] at 30mN (O)	11.1 ± 0.3		
Roa et al.	Y-123/Y-211[6] at 100mN (O)	8.9 ± 0.2	Nanoindentation (Berkovich)	2007
Roa et al.	Y-123[6] at 5mN (T)	11.9 ± 0.7		2008a, b
	Y-211[6] at 5mN (T)	17.9 ± 1.1		
	Y-123/Y-211[6] at 5mN (T)	15.4 ± 0.9		
	Y-123[6] at 10mN (T)	10.2 ± 0.7		
	Y-211[6] at 10 mN (T)	17.0 ± 0.9		
	Y-123/Y-211[6] at 10 mN (T)	14.8 ± 0.4		
	Y-123/Y-211[6] at 30 mN (T)	8.3 ± 0.2		
	Y-123/Y-211[6] at 100 mN (T)	8.1 ± 0.5		
Foerster et al.	YBCO-TSMG (*ab*-plane)	8	Nanoindentation	2008
	YBCO-TSMG (*ca(b)*-plane)	7		
	YBCO-TSMG + 5% Ag_2O (*ab*-plane)	≅ 9		
	YBCO-TSMG + 5% Ag_2O (*ca(b)*-plane)	≅ 8		
	YBCO-TSMG + 10% Ag_2O (*ab*-plane)	≅ 6.5		
	YBCO-TSMG + 10% Ag_2O (*ca(b)*-plane)	≅ 7		

Table 2. Literature values of *H* for $YBa_2Cu_3O_{7-x}$ obtained by indentation techniques.

[6] *Texture process:* Bridgman technique

Author	Material	H (GPa)	Method	Year
	YBCO-TSMG + 15% Ag_2O (*ab*-plane)	≅ 6.5		
	YBCO-TSMG + 15% Ag_2O (*ca(b)*-plane)	≅ 6		
	YBCO-TSMG + 5% Ag_2O	5.2 ± 0.2	Microindentation (Vickers)	
	YBCO-TSMG + 10% Ag_2O	4.1 ± 0.4		
Bartolomé et al.	YBCO[7] (T)	10.6 ± 0.4	Nanoindentation (Berkovich)	2010a
	YBCO[7] (O)	7.6 ± 0.4		
	YBCO weld (0° misorientation) (T)[8]	9.5 ± 0.3		
	YBCO weld (14° misorientation) (T) [8]	6.5 ± 0.4		
	YBCO weld (0° misorientation) (O) [8]	6.8 ± 0.5		
	YBCO weld (14° misorientation) (O) [8]	4.4 ± 0.5		
	YBCO weld (15° misorientation) (O) [8]	5.2 ± 0.3		
Roa et al.	YBCO[7] (O)	8.8 ± 0.3	Nanoindentation	2011b
Roa et al.	YBCO-TSMG (T)	10.5 ± 0.1	Nanoindentation (Berkovich)	2011c
	YBCO-TSMG (O)	7.8 ± 0.1		

Table 2. Literature values of *H* for YBCO obtained by indentation techniques. (continuation)

Author	Material	K_{IC} (MPa $m^{1/2}$)	Method	Year
Lenblond-Harnois et al	YBCO	1.53	Vickers Indentation	2000
	Y-123 + 5% wt Ag	1.88		
Li et al.	MTG-1100ºC, 5min	1.9		1997
	MTG-1100ºC, 10min	1.7		
	MTG-1100ºC, 15min	1.7		
	Solid State Reaction	1.3		
Yoshino et al.	YBCO 40K	0.4		2001
	YBCO 293K	1.3		
Lenders et al.	Y-123 + 30 mol% Y-211	1.01	Vickers Indentation	1999
	Y-123 + 60 mol % Y-211	1.44		
Cook et al.	YBCO	1.10		1998
Foerster et al.	YBCO-TSMG pure	1.43 ± 0.02	Vickers Indentation	2008
	YBCO-TSMG + 10% Ag_2O	1.6 ± 0.1		
Fujimoto et al.	Textured	0.99-1.20	Vickers Indentation	1992
	Y-123 with Ag	1.60-2.10		

Table 3. Literature values of toughness fracture, K_{IC}, for $YBa_2Cu_3O_{7-x}$ obtained by indentation techniques.

[7] *Texture process:* TSMG technique
[8] Hardness value in the welding region (YBCO/Ag/YBCO)

Author	Material	σ_{ys} (GPa)	Method	Year
Roa et al.	YBCO-Bridgman	3.2	Nanoindentation (Spherical)	2010b
Roa et al.	YBCO-TSMG	3.58 ± 0.10		2009c

Table 4. Literature values of yield stress, σ_{ys}, for $YBa_2Cu_3O_{7-x}$ obtained by indentation techniques.

1.2.3 Mechanical properties

The elastic modulus values reported by Roa et al. (Roa et al., 2007, 2009d, 2011b) presented in **Table 1** for Bridgman and TSMG texture processes present a dependency with the applied load. This phenomenon is far from what are expected, as elastic modulus is an intrinsic property of each material and only depends on its composition. Then, this difference of elastic modulus is able to be attributed to one of the following factors:

- Firstly, the contact area value, which is strongly affected by the presence of macro-/microcracks, porosity, roughness and a wide variety of defects. In order to avoid this effect, the polishing process before the indentation should be carefully done.
- Secondly, the elastic modulus is obtained using the unloading slope of the loading-unloading curve, also denoted as S. If the contact point (indenter-sample) is not well estimated, the S value will be underestimated, yielding to a lower E_{eff}.
- Finally, the β factor could not modify the elastic modulus because it remains equal to 1.034 for each test performed (Oliver et al., 1992).

After considering all the different parameters that can modify the elastic modulus, we believe that the main contribution to change it is the contact area, and then the scattered values presented in the **Table 1** and reported by Roa et al. (Roa et al., 2007, 2008b) are attributed to this effect. Moreover, the Bridgman samples present elastic modulus values higher than for TSMG, as this last presents a higher density of macro- and microcracks, which can produce a relaxation of the elastic deformation range, see **Fig. 15.**

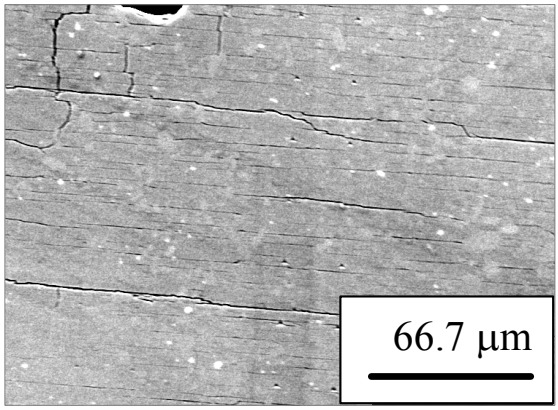

Fig. 15. FE-SEM image of the *ab*-plane of TSMG samples, which present a high microcracks density performed during the oxygenation process due to the tetragonal to orthorhombic transition (from Roa et al., 2011b).

Moreover, the **Table 1** presents several measurements of the elastic modulus for Y-123, which resulted in values scattered within the range between 40 – 200 GPa, caused by residual porosity and bad contact between the grains, as reported Johansen et al. (Johansen et al., 2001). If we compare all the elastic modulus reported in **Table 1**, we can conclude that the broad distribution observed can be attributed to the different measuring techniques (nanoindentation, AFM-FS) and to the different quality of the studied $YBa_2Cu_3O_{7-x}$ samples (grain structure, texture, and others).

Table 2 exhibits the hardness values for $YBa_2Cu_3O_{7-x}$ samples using different techniques. It is well known that the $YBa_2Cu_3O_{7-x}$ samples textured by Bridgman and TSMG techniques present a heterogeneous microstructure with Y-123 matrix and a minor phase (Y-211 or inclusions). Using the conventional micro hardness technique it is not possible to isolate the hardness value for each phase due to that the size of the residual imprint is higher than the size of the different inclusions. However, in 2007, Roa et al. (Roa et al., 2007) using the Nanoindentation technique obtained the hardness value for each phase when the applied load was lower or equal to 10mN. With this applied load, the residual contact area is lower than the size of the inclusions. Then, the mechanical property can be obtained, see **Table 2**. We can observe that the hardness value for Y-211 is around twice times that for Y-123. This fact could be due to different reasons (Roa et al., 2007):

- ionic bond of Y-211 is stronger than Y-123 (related to the different melting point of the two phases, $T_{Y\text{-}123}$ = 1010°C, and $T_{Y\text{-}211}$ = 1200°C (Aselage et al., 1988)),
- high anisotropy of dislocations confined onto a (001) plane (Sandiumenge et al., 2000), and/or
- the melt-processed ceramic composites contain a dense population of fine peritectic particles, which drastically affects the microstructure acting as nucleation sites for dislocations (Sandiumenge et al., 2000).

If the different residual imprints have been performed near the grain boundary, the plastic deformation mechanisms under the imprint could be affected by the Y-123 matrix, and the hardness value would be modified, thus giving us an average of the studied property.

At very small applied loads (lower than 10 mN), the hardness value can be strongly affected by the presence of defects and impurities that can cause almost no change in dislocation movement. In other words, hardness does not remain constant at different applied loads as corroborate Roa *et al.* in 2007 and 2008 (Roa et al., 2007, 2008b). Using Nanoindentation technique this effect can be related to one physical phenomenon known as *Indentation Size Effect*. Normally, hardness presents a maximum value for low loads. However, when the applied load increases this property is widely modified by the superficial defects, such as roughness, macro-cracks, and others. When this phenomenon takes place, the contact area could be over- or underestimated yielding to a false hardness value.

When the applied load using Nanoindentation technique is high (100 mN), overall nanohardness is very similar for both texturing techniques (8.9 GPa and 7.9 GPa for Bridgman and TSMG techniques, respectively). However, these values are lower than the nanohardness value of the Y-123 phase. The different hardness values reported in **Table 2** by Micro or Nanohardness tests at room temperature present the same value at high applied loads. However, when the $YBa_2Cu_3O_{7-x}$ samples are doped with a ductile material as silver oxide, the mechanical response tends to decrease, as reported by Foester et al. (Foester et al.,

2008). Moreover, several studies performed at cryogenic temperature (Güçlü et al., 2005) exhibit that the mechanical properties tend to be higher due to the nitrogen going inside the pre-existing cracks, yielding a homogeneous material. As we can observe in **Table 2,** the different $YBa_2Cu_3O_{7-x}$ samples studied at room temperature are much brittle than at cryogenic temperature due to the effect explained above.

Table 3 shows the different toughness fracture values reported in the literature and obtained using Vickers and Nanoindentation tests. The different results reported in this table present a high scattered due to the $YBa_2Cu_3O_{7-x}$ samples are strongly heterogeneous due to the presence of internal cracks, secondary phases and grain boundaries. Due to all this defects the different toughness values do not present any tendency. Lenblond-Harnois et al. (Lenblond-Harnois et al., 2000) and Foester et al. (Foester et al., 2008) obtained a toughness fracture of 1.88 and 1.6 $MPam^{1/2}$ for $YBa_2Cu_3O_{7-x}$ with 5 and 10% of Ag and Ag_2O, respectively. In that case, this value is higher than the others reported in this table due to the silver introduced inside of the $YBa_2Cu_3O_{7-x}$ samples reduce the fragility of these materials.

Finally, another mechanical parameter to take into account is the yield stress, see **Table 4**. As can be observed in this table, the intrinsic properties obtained using the stress-strain plots present similar values for both samples. The TSMG samples, present a higher density of macro-/microcracks and pore density (see **Fig. 15**) along the *c*-axis than Bridgman samples. Then, during the first contact between the indenter and the samples, the energy applied by the tip onto the surface is employed to close the different cracks produced during the oxygenation process. For this reason, TSMG samples present a higher contact radius value than Bridgman samples.

1.2.4 Fracture mechanisms

In this section we have analysed the different brittle effects appearing in as-grown samples textured by Bridgman and TSMG techniques. **Fig. 16** and **Fig. 17**, show Field Emission Scanning Electron Microscopy images of some residual imprints performed at 10 mN of applied load for Bridgman and TSMG samples, respectively (from Roa et al., 2011b).

All the different imprints in **Fig. 16** present the *sink-in* effect, typically found in elastic, brittle materials (Oliver et al., 1992). Sink-in is an elastic displacement of the surface at the contact perimeter. This effect can lead to an overestimation of the contact area, and thus an underestimation of the hardness value obtained by nanoindentation. As we can observe in this **Figure**, we noted a high density of micrometric pores around the residual imprint. Presumably, this micrometric porosity is created during the recrystalization process. The nanoindentation process would render the pores exposed to the surface, an effect that has been previously described (Gaillard et al., 2008).

In addition, all these images show the presence of microcracks inside the imprints, generated during the indentation process. This kind of damage is found in brittle materials containing inclusions harder than the matrix, in this case Y-211 (see **table 2**). Upon indentation, microcracks tend to be created at inclusions, and are recognised as microflaws within the imprint when observed from the surface.

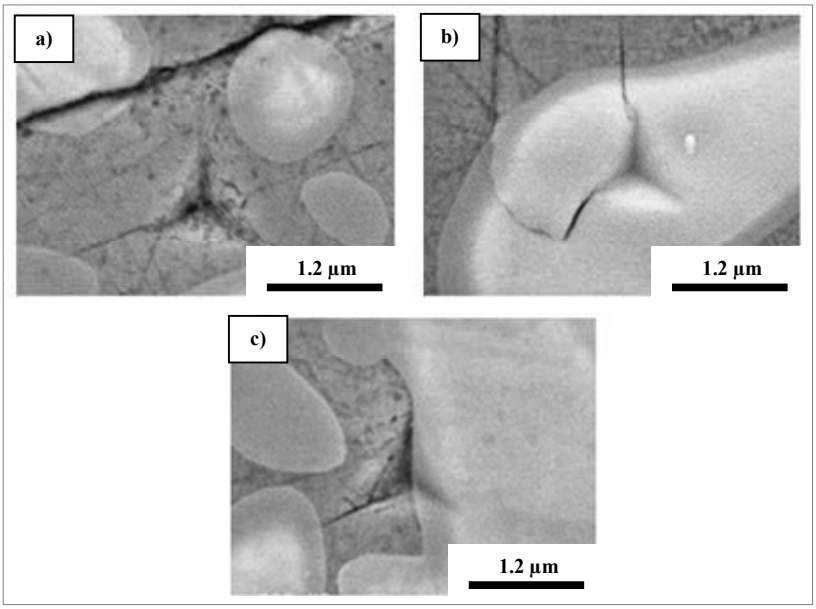

Fig. 16. Micrographs of nanoindentation imprints obtained by FE-SEM when the applied load was 10 mN for Bridgman samples, a) Y-123, b) Y-211 and c) Y-123/Y-211 (from Roa et al., 2011b).

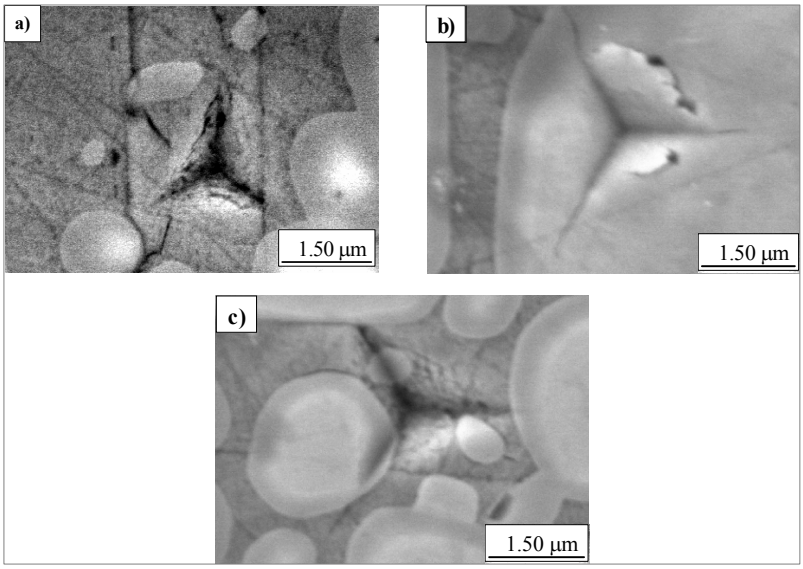

Fig. 17. Micrographs of nanoindentation imprints obtained by FE-SEM when the applied load was 10 mN for TSMG samples, a) Y-123, b) Y-211 and c) Y-123/Y-211 (from Roa et al., 2011b).

Another common feature in all imprints is the presence of radial cracks emanating from the corners of the imprints. This fracture mechanism, typical for ceramic materials, is nucleated due to the tensile strength originated during the indentation process.

Another common fracture mechanism is the *chipping*, i.e. a partial removal of surface material around the imprint. This phenomenon occurs as a result of Palqmvist cracks nucleating at the lateral sides of the imprint, beneath the surface.

In order to understand the fracture mechanisms that take place under the residual imprint, one nanoindentation performed at 10mN has been visualized by FIB, see **Fig. 18** (from Roa et al., 2011b, 2011d).

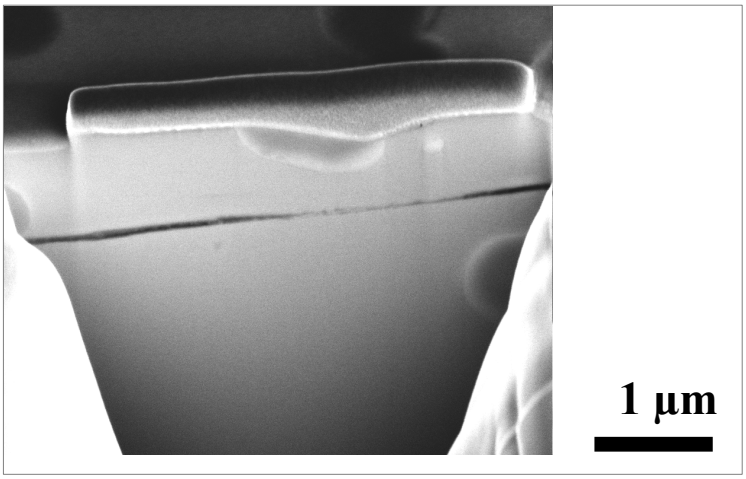

Fig. 18. Cross-sectioning and imaging of damage under an indentation imprint performed at 10mN of applied load in Bridgman samples using FIB-SEM. Cross-sectioning in the middle of the imprint (from Roa et al., 2011d).

Fig. 18 shows a heterogeneous distribution of Y-211 particles around the matrix, with different sizes from 1 to 5 μm. Moreover, no cracks or failure events can be appreciated under the nanoindentation imprint, thus implying that the deformation can be attributed to the closing of the oxygenation micro-cracks. The TSMG samples present the same effect –not shown in this work.

Due to all of these fracture mechanisms, the different values reported in the literature and summarized in the **table 3**, are not reproducible.

2. Conclusions

The paramagnetic Meissner effect has been observed in several superconducting materials grown by different techniques since their discovery, and different models and explanations have been proposed in order to explain their origin. Apparently, there is no a definitive model neither a tendency to saturation and the paramagnetic moments persist up to very high magnetic fields.

The mechanical properties (hardness, elastic modulus, toughness fracture and yield stress) for YBCO samples can be determined using the nanoindentation technique. This technique allows us to isolate the mechanical behavior of each phase, independently of the growing technique used. The mechanical properties for Bridgman samples are higher than that for TSMG samples. This phenomenon can be attributed to the texturing process, as TSMG process creates a high density of macro- and microcracks during the texture and oxygenation steps, respectively.

The values for yield stress for both texturing methods (Bridgman and TSMG), cannot be compared to previous works, as scare information in the literature is available.

With a cross-section, and using FIB technique, we can observe that the samples present a heterogenous distribution of Y-211 particles imbedded in the Y-123 matrix. No generation of porosity or microcracking have been observed, so the deformation mechanisms can be attributed to dislocations movement and twin generation in the *ab*-plane and *c*-axis, respectively.

3. Acknowledgments

The author thanks the Brazilian Ministry of Science and Technology and the State of Rio Grande do Sul, under the Grant PRONEX FAPERGS/CNPq 10/0009-2, and Ministry of Science and Technology, under the Grant CAPES/Procad 059/2007.

4. References

Alcalá, J., Barone, A. C., Anglada, M. (2000). The influence of plastic hardening on surface deformation modes around Vickers and spherical idnents. *Acta Materialia*, Vol. 48, No. 13 pp. 3451-3464

Anderson T. L. (2005). Fracture Mechanics: Fundamentals and Applications. *Taylor & Francis*, ISBN: 978-0-8493-1656-2

Araujo-Moreira, F., Barbara, P., Cawthorne, A., & Lobb, C. (1997). Reentrant ac Magnetic Susceptibility in Josephson-Junction Arrays. *Physical Review Letters,* Vol.78, No.24, (June 1997), pp. 4625-4628, ISSN 0031-9007

Arias, D., Peña, V., Sefrioui, Z., Leon, C., Santamaria, J., Martinez, J., & de la Torre, M. (2006). Paramagnetic Meissner effect in $YBa_2Cu_3O_7/La_{0.7}Ca_{0.3}MnO_3$ superlattices. *Physical Review B,* Vol.73, No.5, (February 2006), pp. 052503-1-4, ISSN 1098-0121

Aselage, T., Keefer, K. (1988). Liquidus relations in Y-Ba-Cu oxides. *Journal of Materials Research*, Vol. 3, pp. 1279-1291

Barbara, P., Araujo-Moreira, F., Cawthorne, A., & Lobb, C. (1999). Reentrant ac magnetic susceptibility in Josephson-junction arrays: An alternative explanation for the paramagnetic Meissner effect. *Physical Review B,* Vol.60, No.10, (September 1999), pp. 7489-7495, ISSN 1098-0121

Bartolomé, E., Roa, J. J., Bozzo, B., Segarra, M., Granados, X. (2010). Effective silver-assisted welding of YBCO blocks : mechanical versus electrical properties. *Superconductor Science and Technology*, Vol. 23, pp. 045013/1-045013/6

Basu, S., Moseson, M. W., Barsoum, M. W. (2006). On the determination of spherical nanoindentation stress-strain curves. *Journal Materials Research*, Vol. 21, Issue 10, pp. 2628-2637

Beegan, D., Maugier, M. T. (2005). Application of composite hardness models to copper thin hardness measurements. *Surface & Coatings Tehcnology*, Vol. 199, pp. 32-37

Blunt, F., Perry, A., Campbell, A., & Siu, R. (1991). An investigation of the appearance of positive magnetic moments on field cooling some superconductors. *Physica C,* Vol.175, No.5/6, (May 1991), pp. 539-544, ISSN 0921-4534

Brandt, D., Binns, C., Gurman, S., Torricelli, G., & Gray, D. (2011). Paramagnetic Meissner transitions in Pb films and the vortex compression model. *Journal of Low Temperature Physics,* Vol.163, No.3-4, (January 2011), pp. 170-175, ISSN 0022-2291

Bräuchle, G., Riedling, S., Lucht, R., Rohberg, K., Lohneysen, H. v., Claus, H., Erb, A., & Müller-Vogt, G. (1994). Observation of the Wohlleben effect in $YBa_2Cu_3O_{7-\delta}$ single crystals. *Physical Review B,* Vol.49, No.18, (May 1994), pp. 13283-13286, ISSN 1098-0121

Braunisch, W., Knauf, N., Kataev, V., Neuhausen, S., Grütz, A., Kock, A., Roden, B., Khomskii, D., & Wohlleben, D. (1992). Paramagnetic Meissner effect in Bi high-temperature superconductors. *Physical Review Letters,* Vol.68, No.12, (March 1992), pp. 1908-1911, ISSN 0031-9007

Burghard, Z., Zimmermann, A., Rödel, J., Aldinger, F., Lawn, B. R. (2004). Crack opening profiles of indentation cracks in normal and anomalous glasses. *Acta Materialia*, Vol. 52, pp. 293-297

Casellas, D., Caro, J., Molas, S., Prado, J. M., Valls, I. (2007). Fracture toughness of carbides in tool steels evaluated by nanoindentation. *Acta Materialia*. Vol. 55, pp. 4277-4286

Choi, Y., Suresh, S. (2003). Nanoindentation of patterned metal lines on a Si substrate. *Scripta Materialia*, Vol. 48, Issue: 3, pp. 249-254

Cook, R. F., Timothy, R. D., Clarke, D. R. (1987). Fracture toughness measurements of $YBa_2Cu_3O_x$ single crystals. *Applied Physics Letters*, Vol. 51, pp. 454-456

Dias, F., Pureur, P., Rodrigues Jr., P., & Obradors, X. (2000). Paramagnetic Meissner effect in melt-textured $YBa_2Cu_3O_{7-\delta}$. *Physica C,* Vol.341-348, No.2, (November 2000), pp. 1377-1378, ISSN 0921-4534

Dias, F., Pureur, P., Rodrigues Jr., P., & Obradors, X. (2004). Paramagnetic effect at low and high magnetic fields in melt-textured $YBa_2Cu_3O_{7-\square}$. *Physical Review B,* Vol.70, No.22, (December 2004), pp. 224519-1-9, ISSN 1098-0121

Dias, F., Vieira, V., de Almeida, M., Falck, A., Pureur, P., Pimentel Jr., J., & Obradors, X. (2010). Paramagnetic Meissner effect at high fields in YCaBaCuO single crystal and melt-textured YBaCuO. *Physica C,* Vol.470, No.1, (December 2010), pp. S111-S112, ISSN 0921-4534

Field, J. S., Swain, M. V. (1993). A simple predictive model for spherical indentation. *Journal of Materials Research*, Vol. 8, Issue: 2, pp. 297-306

Field, J. S., Swain, M. V. (1995). Determining the Mechanical Properties of Small Volumes of Material from Submicron Spherical Indentations. *Journal Materials Research*, Vol. 10, Num. 1 pp. 101-112

Fisher-Cripps, A. C. (1999). The Hertzian contact surface. *Journal of Materials Science*, Vol. 34, No. 1, pp. 129-137

Fischer-Cripps, A. C. (2004). Nanoindentation. *Mechanical Engineering Series. 2nd Edition. Springer.* ISBN 0-387-22045-3

Foester, C. E., Lima, E., Rodriguez, P., Serbena, F. C., Lepienski, C. M., Cantao, M. P., Jurelo, A. R., Obradors, X. (2008). Mechanical properties of Ag-doped top-seeded melt-grown YBCO pellets. *Brazilian Journal of Physics*, Vol. 38, No. 3, pp. 341

Freitag, B., Büchner, B., Knauf, N., Roden, B., Micklitz, H., Freimuth, A., & Kataev, V. (1999). Characteristic microstructure in small Bi-2212 grains showing the Wohlleben effect as revealed by High-Resolution Electron Microscopy. *Europhysics Letters,* Vol.45, No.3, (February 1999), pp. 393-398, ISSN 0295-5075

Fujimoto, H., Murakami, M., Koshizuka, N. (1992). Effect of Y_2BaCuO_5 on fracture toughness of YBCO prepared by a MPMG process. *Physica C*, Vol. 203, Issues 1-2, pp. 103-110

Gaillard, Y., Tromas, C., Woirgard, W. (2006). Quantitative analysis of dislocation pile-ups nucleated during nanoindentation in MgO. *Acta Materialia*, Vol. 54, Issue: 5, pp. 1409-1417

Gaillard, Y., Jiménez-Piqué, E., Soldera, F., Mücklich, F., Anglada, M. (2008). Quantification of hydrothermal degradation in zirconia by nanoindentation. *Acta Materialia*, Vol. 56, Num: 16, pp. 4206-4216

Geim, A., Dubonos, S., Lok, J., Henini, M., & Maan, J. (1998). Paramagnetic Meissner effect in small superconductors. *Nature,* Vol.396, No.6707, (November 1998), pp. 144-146, ISSN 0028-0836

Giese, R. F., Sheahen, T. P., Wolsky, A. M., Sharma, D. K. (1990). High-temperature superconductors; Their potential role in electric utility applications and what must be done to use them. *Proceeding American Conference*, Vol. 52, pp. 776-78

Golovin, Y. I. (2008). Nanoindentation and Mechanical properties of solids in submicrovolumes, thin near-surface layers, and films: a review. *Physics of the Solid State*, Vol. 50, No. 12, (December 2008), pp. 2205-2236, ISSN 1063-7834

Goyal, A., Oliver, W. C., Funkenbusch, P. D., Kroeger, C. M., Burns, S. J. (1991). Mechanical properties of highly aligned $YBa_2Cu_3O_{7-\square}$ effect of Y_2BaCuO_x particles. *Physica C*, Vol. 183, No. 4-6, pp. 221-233

Güçlü, N., Kölemen, U., Uzum, O., Selebi, S. (2005). Work of indentation approach for investigation of mechanical properties of YBCO bulk superconductor at cryogenic temperatures. *Physica C*, Vol. 433, pp. 115-122

Hay, J. C., Bolshakov, A., Pharr, G. M. (1999). Critical Examination of the Fundamental Relations in the Analysis of Nanoindentation Data. *Journal of Materials Research*, Vol. 14, No. 6, pp. 2296-2305

Hertz, H., Reina, Angew, J. Math 92 (1982) 156. (Translated and reprinted in English in Hertz's Miscellaneous Papers, MacMillan and Co., London (1986) Ch. 5)

Jang, J., Pharr, G. M. (2008). Influence of indenter angle on cracking in Si and Ge during nanoindentation. *Acta Materialia*, Vol. 56, pp. 4458-4469

Jiménez-Piqué, E., Gaillard, Y., Anglada, M. (2007). Instrumented Indentation of Layered Ceramic Materials. *Key Enginnering Materials*, Vol. 333, pp. 107-116

Johansen, T. H. (2000). Flux-pinning-induces stress and magnetostriction in bulk superconductors. *Superconductor Science and Technology*, Vol. 13, No. 10, pp. R121

Johnson, K. L. (1985). Contact Mechanics. *Cambridge University Press*, Vol. 176, p. 94

Joo, J., Kim, J. G., Nah, W. (1998). Improvement of mechanical properties of YBCO-Ag composite superconductors made by mixing with metallic Ag powder and $AgNO_3$ solution. *Superconductors Science and Technology*, Vol. 11, No. 7, pp. 645

Khomskii, D. (1994). Wohlleben effect (paramagnetic Meissner effect) in high-temperature superconductors. *Journal of Low Temperature Physics,* Vol.95, No.1/2, (April 1994), pp. 205-223, ISSN 0022-2291

Kim, H., Minami, H., Schmidbauer, W., Hodby, J., Lyo, A., Iga, F. & Uwe, H. (1996). Paramagnetic Meissner effect in superconducting single-crystals of $Ba_{1-x}K_xBiO_3$. *Journal of Low Temperature Physics,* Vol.105, No.3/4, (November 1996), pp. 557-562, ISSN 0022-2291

Koshelev, A., & Larkin, A. (1995). Paramagnetic moment in field-cooled superconducting plates: paramagnetic Meissner effect. *Physical Review B,* Vol.52, No.18, (November 1995), pp. 13559-13562, ISSN 1098-0121

Kostic´, P., Veal, B., Paulikas, A., Welp, U., Todt, V., Gu, C., Geiser, U., Williams, J., Carlson, K., & Klemm, R. (1996). Paramagnetic Meissner effect in Nb. *Physical Review B,* Vol.53, No.2, (January 1996), pp. 791-801, ISSN 1098-0121

Kusmartsev, F. (1992). Destruction of the Meissner Effect in Granular High-Temperature Superconductors. *Physical Review Letters,* Vol.69, No.15, (October 1992), pp. 2268-2271, ISSN 0031-9007

Kusmartsev, F., Rykov, A., & Tajima, S. (1997). High-field paramagnetic effect in large crystals of $YBa_2Cu_3O_{7-\square}$. *Physical Review B,* Vol.55, No.13, (April 1997), pp. 8557-8563, ISSN 1098-0121

Lawn, B. R., Evans, A. G., Marshall, D. B. (1980). Elastic/plastic indentation damage in ceramics: The median/radial crack system. *Journal of the American Ceramic Society*. Vol. 25, pp. 1053-1067

Lawn, B. R., Swain, M. V., Philips, K. (1975). On the mode of chipping fracture in brittle solids. *Journal of Materials Science*. Vol. 10, pp. 1236-1239

Lebed, A. (2008). Paramagnetic intrinsic Meissner effect in layered superconductors. *Physical Review B,* Vol.78, No.1, (July 2008), pp. 012506-1-4, ISSN 1098-0121

Leblond-Harnois, C., Caillard, R., Monot-Laffez, I., Desgardin, G., Raveau, B. (2000). Texturing process, superconducting and mechanical properties of Ag-doped top-seeded melt-grown YBCO pellets. *Physica C*, Vol. 341-348, No. 4, pp. 2439-2440

Leenders, A., Ullrich, M., Freyhardt, H. C., Kesten, M., Fieseler, H., Canders, W. R., May, H., Bock, J. (1999). Fabrication of HTS monoliths for a bearing system in a cryogenic vessel. *IEEE Transactions on Applied Superconductivity*, Vol. 9, Issue 2, pp. 992-995

Leenders, A., Ullrich, M., Freyhardt, H. C. (1999). Mechanical properties of TSMG-YBCO. *IEEE Transaction on Applied Superconductivity*, Vol. 9, Issue 2, pp. 2074-2077

Li, M. (2003). Paramagnetic Meissner effect and related dynamical phenomena. *Physics Reports,* Vol.376, No.3, (March 2003), pp. 133-223, ISSN 0370-1573

Li, L. F., Zhang, Z., Jin, D., Li, Y. Y., Meriani, S. (1997). Microstructure and mechanical properties of MTG YBCO. *Physica C*, Vol. 282-287, No. 4, pp. 2599-2600

Lim, Y. Y., Chaudhri, M. M. (2001). Do residual nanoindentations in metals and ceramics relax with time?. *Journal of Physics D: Applied Physics*, Vol. 34, L70-L78

Lucas, B. N., Oliver, W. C., William, R. K., Brynestad, J., O'Hern, M. E. (1991). The Hardness and Young's modulus of Bulk $YBa_2Cu_3O_{7-x}$ (1:2:3) and $YBa_2Cu_4O_8$ (1:2:4) as Determined by Ultra Low Load Indentation. *Journal Materials Research*, Vol. 6, pp. 2519-2522

Lucas, B. N., Oliver, W. C., Swindeman, J. E. (1998). The Dynamics of Frequency-Specific, Depth-Sensing Indentation Testing, Fundamentals of Nanoindentation and Nanotribology. *Materials Research Society Symposium Proc*. Vol. 522, pp. 3-14

Lucht, R., Löhneysen, H., Claus H., Kläser, M., & Müller-Vogt, G. (1995). Surface-sensitive paramagnetic Meissner effect in $YBa_2Cu_3O_x$ single crystals. *Physical Review B,* Vol.52, No.13, (October 1995), pp. 9724-9726, ISSN 1098-0121

Magnusson, J., Anderson, J., Björnander, M., Nordblad, P., & Svedlindh, P. (1995). Time dependence of the paramagnetic Meissner effect: Comparison between model calculations and experiments. *Physical Review B,* Vol.51, No.18, (May 1995), pp. 12776-12781, ISSN 1098-0121

Minhaj, M., Thompson, D., Wenger, L., & Chen, J. (1994). Paramagnetic Meissner effect in a niobium disk. *Physica C,* Vol.235/240, No.4, (December 1994), pp. 2519-2520, ISSN 0921-4534

Moseson, A. J., Basu, S., Barsoum, M. W. (2008). Determination of the effective zero point of contact for spherical nanoindentation. *Journal Materials Research*, Vol. 23, No. 1, pp. 204-209

Moshchalkov, V., Qiu, X., & Bruyndoncx, V. (1997). Paramagnetic Meissner effect from the self-consistent solution of the Ginzburg-Landau equations. *Physical Review B,* Vol.55, No.17, (May 1997), pp. 11793-11801, ISSN 1098-0121

Nielsen, A., Cawthorne, A., Barbara, P., Wellstood, F., Lobb, C., Newrock, R., & Forrester, M. (2000). Paramagnetic Meissner effect in multiply-connected superconductors. *Physical Review B,* Vol.62, No.21, (December 2000), pp. 14380-14383, ISSN 1098-0121

Nordblad, P., Magnusson, J., Papadopoulou, E., & Svedlindh, P. (1998). ac susceptibility of a paramagnetic Meissner effect sample. *Physica C,* Vol.297, No.3-4, (March 1998), pp. 317-325, ISSN 0921-4534

Obukhov, Y. (1998). The "Paramagnetic" Meissner Effect in Superconductors. *Journal of Superconductivity,* Vol.11, No.6, (July 1998), pp. 733-736, ISSN 0896-1107

Oliver, W. C., Pharr, G. M. (1992). An improved Technique for Determining Hardness and Elastic Modulus Using load and Displacement Sensing Indentation Experiments. *Journal of Materials Research*. Vol. 7, No. 6, pp. 1564-1583

Oliver, W. C., Pharr, G. M. (2004). Measurement of hardness and elastic modulus by instrumented indentation: Advances in understanding and refinements to methodology. *Journal Materials Research*, Vol. 19, Issue 1, pp. 3-20

Pan, A., Luzhbin, D., Komashko, V., Flis, V., Pan, V., Dou, S., & Esquinnazi, P. (2004). Origin of paramagnetic magnetization in field-cooled $YBa_2Cu_3O_{7-\square}$ films. *Physical Review B,* Vol.69, No.2, (January 2004), pp. 024506-1-7, ISSN 1098-0121

Pethica, J. B., Oliver, W. C. (1989). Mechanical Properties of Nanometer Volumes of Material: Use of the Elastic Response of Small Area Indentations, in Thin Films-Stresses and Mechanical Properties. *Materials Research Society Symposium Proc*. Vol. 130, pp. 13-23

Pharr, G. M.., Oliver, W. C., Brotzen, F. R. (1992). On the generality of the relationship among contact stiffness, contact area and elastic modulus during indentation. *Journal of Materials Research*, Vol. 7, pp. 613-617

Pureur, P., Dias, F., Rodrigues Jr., P., & Obradors, X. (2001). Paramagnetic Meissner effect at high fields in melt-textured $YBa_2Cu_3O_{7-\delta}$. *Physica C,* Vol.354, No.1-4, (May 2001), pp. 219-222, ISSN 0921-4534

Rayon, E., Bonache, V., Salvador, M. D., Roa, J. J., Sanchez, E. (2011). Hardness and Young's modulus distributions in atmospheric plasma sprayed WC-Co coatings using nanoindentation. *Surface & Coatings Tehcnology*, Vol. 205, pp. 4192-4197

Roa, J. J., Capdevila, X. G., Martinez, M., Espiell, F., Segarra, M. (2007). Nanohardness and Young's modulus of YBCO samples textured by the Bridgman technique. *Nanotechnology*, Vol. 18, pp. 385701/1-385701/6

Roa, J. J., Jiménez-Piqué, E., Capdevila, X. G., Martinez, M., Segarra, M. (2008a). Yield strength, shear stress and toughness of YBCO samples textured by Bridgman technique. *Journal of Physics: Conference Series*, Vol. 97, pp. 012116/1-012116/6

Roa, J. J., Capdevila, X. G., Segarra, M. (2008b). Estudio de los Mecanismos de Fractura durante la oxigenacion del YBCO. *Anales de Mecanica de la fractura 25*, Vol. 1, pp. 55-60

Roa, J. J., Gilioli, E., Bissoli, F., Pattini, F., Rampino, S., Capdevila, X. G., Segarra, M. (2009a). Study of the mechanical properties of CeO_2 layers with the nanoindentation technique. *Thin Solid Films*, Vol. 518, pp. 227-232

Roa, J. J., Dias, F. T., Vieira, V. N., Oncins, G., Diaz, J., Schaf, J., Capdevila, X. G., Segarra, M. (2009b). Caracterizacion mecanica a escala picometrica de $YBa_{1.75}Sr_{0.25}Cu_3O_{7-\delta}$ monocristlaino mediante la tecnica de autoflujo. *Anales de Mecanica de la Fractura* 26, Vol. 2, pp. 489-494

Roa, J. J., Morales, M., Martinez, M., Capdevila, X. G., Segarra, M. (2009c). Curva tension-deformacion mediante indentacion esferica para materiales ceramicos superconductores de YBCO-TSMG. *Anales de Mecanica de la Fractura 26*, Vol. 2, pp. 495-500

Roa, J. J., Capdevila, X. G., Segarra, M. (2009d). Mechanical characterization at Nanometric Scale of Cermic Superconductor Composites. *Superconducting Magnets and Superconductivity: Research, Technology and Applications; Publisher: Nova Science Publishers, Chapter 3.* pp. 77-168. ISBN: 978-1-60741-017-1

Roa, J. J., Bartolomé, E., Bozzo, B., Capdevila, X. G., Granados, X., Segarra, M. (2010a). Nano-mechanical properties of silver-welded YBCO bulks. *Journal of Physics: Conference Series*, Vol. 234, pp. 012034/1-012034/6

Roa, J. J., Jiménez-Piqué, E., Capdevila, X. G., Segarra, M. (2010b). Nanoindentation with spherical tips of single crystals of YBCO textured by the Bridgman technique: Determination of indentation stress-strain curves. *Journal of the European Ceramic Society*, Vol. 30, pp. 1477-1481

Roa, J. J., Capdevila, X. G., Segarra, M. (2010c). Mechanical characterization at Nanometric Scale of Cermic Superconductor Composites. *Nanotechnology: Nanofabrication, Patterning and Self Assembly; Publisher: Nova Science Publishers, Chapter 5.* pp. 151-236. ISBN: 978-1-60692-162-3

Roa, J. J., Jiménez-Piqué, Puig, T., Obradors, X., Segarra, M. (2011a). Nanoindentation of multilatered epitaxial $YBa_2Cu_3O_{7-\delta}$ thin films and coated conductors. *Thin Solid Films*, Vol. 519, pp. 2470-.2476

Roa, J. J., Segarra., M. (2011b). Mechanical properties of HTSC. *Publisher: Lambert Academic Publishing*. ISBN: 978-3-8465-0957-9

Roa, J. J., Dias, F. T., Martinez, M., Padilla, J. A., Segarra, M. (2011c). Oxygenation Kinetics of YBCO-TSMG samples using the nanoindentation technique. *Journal of the European Ceramic Society*. DOI: 10.1016/j.jeurceramsoc.2011.09.013

Roa, J. J., Kosntantopoulou, K., Jiménez-Piqué, E., Martin, V., Segarra, M., Pastor, J. Y. (2011d). Nanoindentation of Bridgman YBCO samples. *Ceramics International*. DOI: 10.1016/j.ceramint.2011.10.039

Roa, J. J., Oncins, G., Dias, F. T., Vieira, V. N., Schaf, J., Segarra, M. (2011e). AFM as an alternative for Young's modulus determination in ceramic materials in elastic deformation range. *Physica C*, Vol. 471, pp. 544-548

Roa, J. J., Oncins, G., Diaz, J., Capdevila, X. G., Sanz, F., Segarra, M. (2011f). Study of the friction, adhesion and mechanical properties of single crystals, ceramics and ceramic coatings. *Journal of the European Ceramic Society*, Vol. 31, pp. 429-449

Roa, J. J., Oncins, G., Diaz, J., Sanz, F., Segarra, M. (2011g). Calculation of Young's modulus Value by Means of AFM. *Recent Patents on Nanotechnology*, Vol. 5, pp. 27-36

Rotoli, G., De Leo, C., Barbara, P., Nielsen, A., & Lobb, C. (2001). Mutual-inductance route to the paramagnetic Meissner effect in two-dimensional Josephson-junction arrays. *Physical Review B,* Vol.64, No.14, (September 2001), pp. 144518-1-5, ISSN 1098-0121

Sandiumenge, F., Puig, T., Rabier, J., Plain, J., Obradors, X. (2000). Optimization of Flux Pinning in Bulk Melt Textured 1-2-3 Superconductors: Bringing Dislocations under Control. *Advanced Materials*, Vol. 12, Issue 5, pp. 375-381

Schwartz, A., Chu, S., Massalski, T., & Laughlin, D. (2006). Extrinsic paramagnetic Meissner effect in multiphase indium-tin alloys. *Applied Physics Letters,* Vol.89, No.11, (September 2006), pp. 111903-1-3, ISSN 1077-3118

Sigrist, M., & Rice, T. (1995). Unusual paramagnetic phenomena in granular high-temperature superconductors - A consequence of *d*-wave pairing? *Review of Modern Physics,* Vol.67, No.2, (April 1995), pp. 503-513, ISSN 0034-6861

Svedlindh, P., Niskanen, K., Norling, P., Nordblad, P., Lundgren, L. Lönnberg, B., & Lundström, T. (1989). Anti-Meissner effect in the BiSrCaCuO-system. *Physica C,* Vol.162/164, No.2, (December 1989), pp. 1365-1366, ISSN 0921-4534

Svedlindh, P., Papadopoulou, E., Nordblad, P., Schöneberger, R., & Gross R. (1999). Magnetic Aging in $Bi_2Sr_2CaCu_2O_8$ Displaying the Paramagnetic Meissner Effect. *Physical Review Letters,* Vol.82, No.1, (January 1999), pp. 173-176, ISSN 0031-9007

Terentiev, A., Watkins, D., De Long, L., Morgan, D., & Ketterson, J. (1999). Paramagnetic relaxation and Wohlleben effect in field-cooled Nb thin films. *Physical Review B,* Vol.60, No.2, (July 1999), pp. R761-R764, ISSN 1098-0121

Thompson, D., Wenger, L., & Chen, J. (1996). Paramagnetic Meissner effect in conventional Nb superconductors. *Journal of Low Temperature Physics,* Vol.105, No.3/4, (November 1996), pp. 509-514, ISSN 0022-2291

Tsui, T. Y., Oliver, W. C., Pharr, G. M. (1997). Indenter Geometry Effects on the Measurement of Mechanical Properties by Nanoindentation with Sharp Indenters, in Thin Films-stresses and Mechanical Properties VI. *Materials Research Society Symposium Proc.*, Vol. 436, pp. 147-152

Wortiz, W., Lisboa-Filho, P., Passos, W., & Araújo-Moreira, F. (2001). Field-induced networks of weak-links: an experimental demonstration that the paramagnetic Meissner effect is inherent to granularity. *Physica C,* Vol.361, No.4, pp. 267-273, ISSN 0921-4534

Yoshino, Y., Iwabuchi, A., Noto, K., Sakai, N., Murakami, M. (2001). Vickers hardness properties of YBCO bulk superconductor at cryogenic temperatures. *Physica C*, Vol. 357-360, pp. 796-798

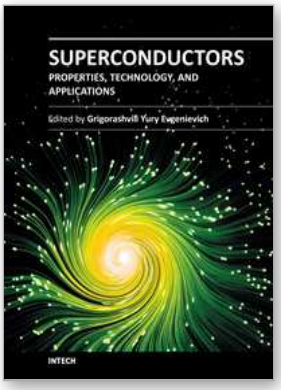

Superconductors - Properties, Technology, and Applications
Edited by Dr. Yury Grigorashvili

ISBN 978-953-51-0545-9
Hard cover, 436 pages
Publisher InTech
Published online 20, April, 2012
Published in print edition April, 2012

Book "Superconductors - Properties, Technology, and Applications" gives an overview of major problems encountered in this field of study. Most of the material presented in this book is the result of authors' own research that has been carried out over a long period of time. A number of chapters thoroughly describe the fundamental electrical and structural properties of the superconductors as well as the methods researching those properties. The sourcebook comprehensively covers the advanced techniques and concepts of superconductivity. It's intended for a wide range of readers.

How to reference
In order to correctly reference this scholarly work, feel free to copy and paste the following:

J.J. Roa, F.T. Dias and M. Segarra (2012). Magnetical Response and Mechanical Properties of High Temperature Superconductors, YBaCu3O7-X Materials, Superconductors - Properties, Technology, and Applications, Dr. Yury Grigorashvili (Ed.), ISBN: 978-953-51-0545-9, InTech, Available from: http://www.intechopen.com/books/superconductors-properties-technology-and-applications/review-magnetical-response-and-mechanical-properties-of-second-generation-htsc-ybco-materials

INTECH
open science | open minds

InTech Europe
University Campus STeP Ri
Slavka Krautzeka 83/A
51000 Rijeka, Croatia
Phone: +385 (51) 770 447
Fax: +385 (51) 686 166
www.intechopen.com

InTech China
Unit 405, Office Block, Hotel Equatorial Shanghai
No.65, Yan An Road (West), Shanghai, 200040, China
中国上海市延安西路65号上海国际贵都大饭店办公楼405单元
Phone: +86-21-62489820
Fax: +86-21-62489821

© 2012 The Author(s). Licensee IntechOpen. This is an open access article distributed under the terms of the Creative Commons Attribution 3.0 License, which permits unrestricted use, distribution, and reproduction in any medium, provided the original work is properly cited.